

Flavin Mononucleotide-Mediated Formation of Highly Electrically Conductive Hierarchical Monoclinic Multiwalled Carbon Nanotube-Polyamide 6 Nanocomposites

Minsuk Park, Seulki Yoon, Junmo Park, No-Hyung Park,* and Sang-Yong Ju*



Cite This: *ACS Nano* 2020, 14, 10655–10665



Read Online

ACCESS |



Metrics & More



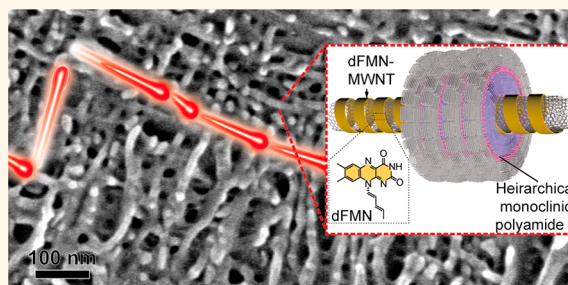
Article Recommendations



Supporting Information

ABSTRACT: Although the multiwalled carbon nanotube (MWNT) is a promising material for use in the production of high electrical conductivity (σ) polymer nanocomposites, its tendency to aggregate and distribute randomly in a polymer matrix is a problematic issue. In the current study, we developed a highly conductive and monoclinically aligned MWNT-polyamide 6 (PA) nanocomposite containing interfacial flavin moieties. In this system, the flavin mononucleotide (FMN) initially serves as a noncovalent aqueous surfactant for individualizing MWNTs in the form of FMN-wrapped MWNTs (FMN-MWNT), and then partially decomposed FMN (dFMN) induces crystallization of the PA on the MWNTs. The results of experiments performed using material subjected to partial dissolution of PA matrix show that the nanocomposite PA-dFMN-MWNT, formed by melt extrusion of PA and dFMN-MWNT, contains a three-dimensional monoclinic MWNT network embedded in an equally monoclinic PA matrix. An increase in monoclinic network promoted by an increase in the content of MWNT increases σ of the nanocomposite up to 100 S/m, the highest value reported for a polymer-MWNT nanocomposite. X-ray diffraction along with transmission electron microscopy reveal that the presence of dFMN induces the formation of monoclinic PA on dFMN-MWNT. The high σ of the PA-dFMN-MWNT nanocomposite is also a consequence of a minimization of defect formation of MWNT by noncovalent functionalization. Hierarchical structural ordering, yet individualization of MWNTs, provides a viable strategy to improve the physical property of nanocomposites.

KEYWORDS: polyamide 6, multiwalled carbon nanotube, nanocomposite, flavin mononucleotide, electrical conductivity, hierarchy, crystallization



Because of its large electrical conductivity (σ), associated with a π -conjugated carbon honeycomb cylinder with a high aspect ratio exceeding 100, the multiwalled carbon nanotube (MWNT)¹ has been employed in electrical materials for several purposes including electromagnetic shielding,^{2–7} transparent conductive coating,⁸ and optoelectronic sensing.^{9–11} However, fabrication of highly conductive MWNT nanocomposites is a major challenge because it is difficult to generate uniformly distributed individualized and aligned MWNT networks in matrix polymers.^{12,13} To overcome the low σ issue created by bundling, a MWNT containing or lacking covalent or noncovalent functionality is dispersed in various solvents prior to mixing with the polymeric matrix. Functionalization of either or both the MWNT or polymer matrix is often employed to improve adhesion at interfaces.¹⁴ Chemical sites for covalent functionalization of MWNT include carboxyl, amine, and hydroxyl groups, which are

often introduced by using a harsh treatment with strong acids, such as a mixture of sulfuric and nitric acids.^{15,16} However, covalent functionalization unavoidably leads to deterioration of the intrinsic electrical properties of the MWNT. An alternative approach, which avoids this issue, involves noncovalent functionalization of the MWNT with poly(flourene) (PFO).¹⁷ This process leads to nanocomposites that have enhanced electrical properties because the surfactants cause strong interactions between the backbone of the polymer

Received: June 22, 2020

Accepted: August 3, 2020

Published: August 3, 2020



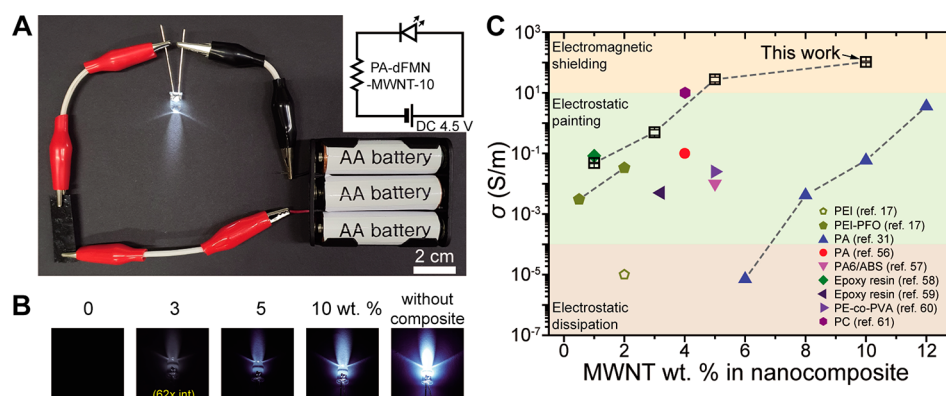


Figure 2. PA-dFMN-MWNT nanocomposites σ measurements. (A) Photograph of a circuit comprised of LED, 4.5 V AA batteries, and PA-dFMN-MWNT as an electrical conductor. Inset: circuit diagram. (B) Photographs of A LED in circuits containing PA-dFMN-MWNT with an increasing wt % of MWNT. Photographs were taken using a shutter speed of 1/250 s unless otherwise noted. (C) The σ values of PA-dFMN-MWNT-1, -3, -5, and -10 and those of previously prepared polymer-MWNT nanocomposites. Error bars in σ were obtained from the standard deviation using three separate measurements. Shaded parts are for the various applications.

highest value for a polymer-MWNT nanocomposite observed thus far. The high σ of the three-dimensional monoclinic MWNT structure of PA-dFMN-MWNT is a consequence of two important features: One is the dFMN promoted creation of a monoclinic PA matrix interlocked with monoclinic PA on MWNT. Second, the results of Raman spectroscopy show that the high σ also results from the preservation of the sp^2 hybridized structure of MWNT by noncovalent functionalization.

RESULTS AND DISCUSSION

Preparation of Nanocomposites PA-dFMN-MWNT.

The two-step procedure developed for fabricating highly electrically conductive NMNT nanocomposites is portrayed in a schematic manner in Figure 1A–C. In the first step, the water-soluble surfactant FMN is utilized in a previously developed procedure^{40,42} to individualize the MWNTs. In this process, ball milling of MWNT with a diameter of 11 nm in an aqueous FMN solution for 1 h (see Methods) leads to production of a MWNT in a black slurry, which is separated by filtration, washed with a copious amount of water, and lyophilized to produce individualized FMN-MWNT as a black powder. In the debundling process, the aromatic isoalloxazine ring in FMN helically wraps around the MWNT, and repulsion of the radially distributed anionic *d*-ribityl phosphate group causes the modified MWNT to form a good colloidal anionic dispersion.⁴⁰ Although the phosphate group in the FMN side chain serves as the repulsive driving force for individualization of the MWNTs, its hydrophilic nature makes it incompatible with nanocomposite formation owing to the presence of hydrophobic methylene chains in the PA polymer. As a result, a second step involving annealing at 450 °C under an air atmosphere is performed to produce a modified form dFMN-MWNT that is compatible with the PA matrix (Figure 1B). Importantly, the annealing processes promote partial decomposition of the highly polar and negatively charged FMN side chain of FMN to mainly create a modified *N*-pentadienyl isoalloxazine form (dFMN).⁴² The structures of MWNT and the isoalloxazine ring (orange color) remain intact in the annealing step, as evidenced by the observation of a quasi-periodic average 1 nm height of the helical wrapping of dFMN on MWNT by using atomic force microscopy (AFM) (see representative images in Figure S1A,B

in the Supporting Information (SI)). This contrasts with the average 2 nm height undulation observed for *d*-ribityl phosphate containing FMN-MWNT.⁴² The results of thermogravimetric analysis (TGA) indicate that FMN displays weight losses at 290 and 450 °C (Figure S2A) which are attributed to dehydroxylation followed by dephosphorylation of the *d*-ribityl phosphate group, respectively.^{42,54} In contrast, the findings show that dFMN remains unchanged below 350 °C but undergoes a 21% weight loss at 524 °C owing to the decomposition of *N*-pentadienyl isoalloxazine group into an alloxazine. This change, which is in good agreement with the calculated weight loss (*i.e.*, 20.9%), is employed to determine that the 96.6 wt % of dFMN remains in dFMN-MWNT (Figure S2B) and that dFMN-MWNT contains 16.3% of dFMN.

MWNT containing nanocomposites PA-dFMN-MWNT-1, -3, -5, and -10 were prepared by melt extrusion of mixtures of PA and 1, 3, 5, and 10 wt % dFMN-MWNT, respectively. Mixing was performed by utilizing a twin-screw melt extruder at 250 °C (Figure 1C), which is approximately 30 °C higher than the melting point of PA. Then, a hot press was employed to generate nanocomposite sheets with thicknesses in the range of 90–405 μ m for electrical and mechanical measurements. As can be seen by viewing the photographs displayed in Figure 1D, the color of the PA-dFMN-MWNT nanocomposite changes from off-white to black as the MWNT content increases.

Electrical Property Measurements of Nanocomposites. The results of electrical conductivity studies showed that the σ values of PA-dFMN-MWNT sheets increase as the MWNT content increases. This conclusion arises from experiments in which the nanocomposites are connected in series to a light-emitting diode (LED) connected to 4.5 V AA batteries (Figure 2A). As can be seen by viewing the photographs in Figure 2B, the light intensity of LED in this system becomes progressively more intense as the wt % of MWNT in the nanocomposite increases. The results of four-probe electrical measurements (Figure 2C) demonstrated that the composites have increasing σ values that reach a maximum of 104 S/m \pm 6 S/m for PA-dFMN-MWNT-10, which is suitable for an electromagnetic shielding application. This value is nearly 10 times higher than those observed to date for various polymer-based MWNT nanocomposites, including

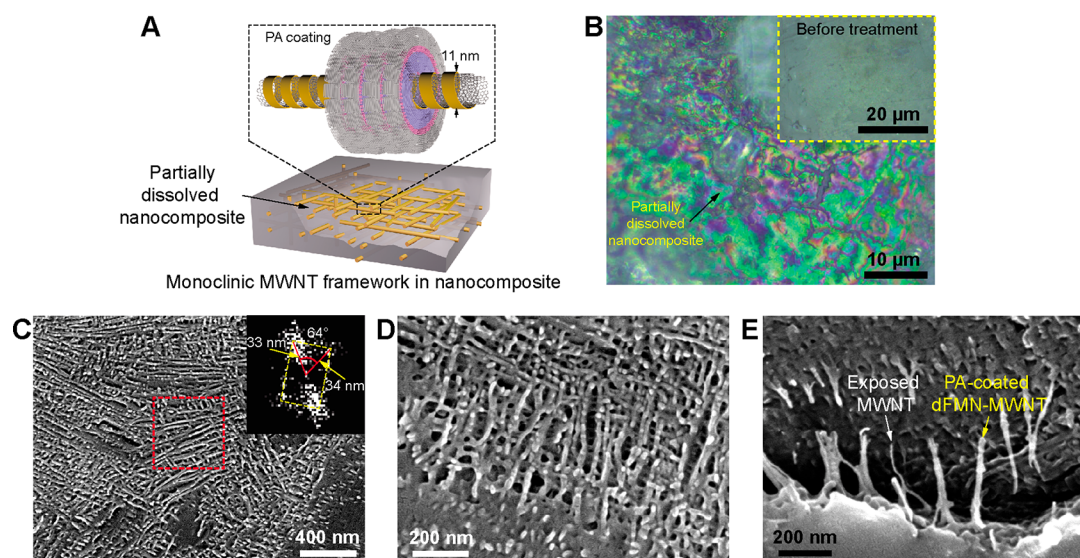


Figure 3. MWNT morphology embedded in PA after hot xylene treatment. (A) Schematic illustration of crystalline PA on dFMN-MWNT-10 after hot xylene treatment. (B) OM image of nanocomposite surface after hot xylene treatment. Inset: Image of the nanocomposite prior to the treatment. SEM images of monoclinic MWNT network with (C) low and (D) high magnifications. Inset: FT image of selected area (red dash) of (C). (E) SEM image of PA-coated dFMN-MWNT (yellow arrow) and exposed dFMN-MWNT (white arrow) in a microcrack region.

poly(ether imide) (PEI),¹⁷ PEI-PFO,¹⁷ PA,^{31,55} PA/poly-(acrylonitrile-butadiene-styrene) (ABS),⁵⁶ epoxy resin,^{57,58} poly(ethylene-co-vinyl acetate) (PE-co-PVA),⁵⁹ and polycarbonate (PC) (Figure 2C).⁶⁰ Moreover, the σ of PA-dFMN-MWNT-10 is 2 orders of magnitude higher than those of similar PA-based nanocomposites having similar MWNT contents.^{31,55} Although nanocomposites with $\sigma > 100$ S/m have been developed previously, their designs are based on surface coating⁶¹ or an addition of conductive ionic liquid,⁶² which are different from PA-dFMN-MWNT-10 which is bulk nanocomposite.

Investigation of MWNT Alignment in the PA Matrix.

To obtain information about the origin of the high σ values, surface morphologies of PA-dFMN-MWNT-1, -5, and -10 were assessed by using SEM (Figure S3A–F). The results showed that the surface of PA-dFMN-MWNT-1 (Figure S3A) contains an intermittent white MWNT-enriched domain (indicated by the yellow enclosed area) surrounded by the PA matrix. A closer inspection (Figure S3B) of the SEM image reveals that the white domain contains uniform PA-MWNT studs with a uniform diameter of *ca.* 100 nm. Considering the diameter of the MWNTs, this finding suggests that a *ca.* 45 nm-thick layer of PA coats the MWNT surface in a sheath-core structural manner during melt extrusion. This observation shows that dFMN on MWNT enables a good adhesion to PA because in the absence of adhesion, only a bare MWNT would be seen protruding from nanocomposite surface. Inspection of SEM images of the surfaces of PA-dFMN-MWNTs containing higher MWNT contents (Figure S3C–F) shows that they have “coral”-like MWNT features and that nanocomposites become a macroscopic continuous phase.

The next stage of this effort focused on how the structural network of the MWNT in PA-dFMN-MWNT is oriented in the PA matrix. For this purpose, PA-dFMN-MWNT-10 was treated with *p*-xylene at 100 °C for 30 min, a condition which is adequate to dissolve the surface PA matrix and expose the MWNT skeleton. Inspection of the optical microscope (OM) image (Figure 3B) shows that the exposed surface exhibits an interference pattern which is generally associated with the

presence of a superlattice structure.⁶³ Importantly, the surfaces of PA-dFMN-MWNT-10 before exposure to hot *p*-xylene (inset) and that of PA and xylene-treated PA (Figure S4A–D) do not display similar interference patterns. Interestingly, viewing the SEM image given in Figure 3C shows that hot xylene-treated PA-dFMN-MWNT-10 has a monoclinically packed MWNT structure, which contrasts sharply with entangled texture of individualized MWNT in dFMN-MWNT (Figure S5A–D). A representative Fourier-transform (FT) image (inset in Figure 3C) shows that this nanocomposite has a monoclinic pattern with a center-to-center spot spacing of *ca.* 33–34 nm, which originates from the thickness of PA-dFMN-MWNT, and a contained angle of 64°, suggesting the existence of a hierarchical MWNT structure embedded in PA. Other areas of the surface also display a monoclinic spacing with spot spacings of *ca.* 33–46 nm and contained angles of 64–83° (see FT images in Figure S6A–F). This type of monoclinic packing of the MWNTs does not occur in other PA-MWNT nanocomposites.^{31,64} Moreover, such structural anisotropy might cause a σ difference in vertical and horizontal directions. When anisotropic σ measurements of PA-dFMN-MWNT-10 with a two-probe method were conducted, vertical σ is *ca.* 1.7 times higher than horizontal σ , showing a slightly anisotropic σ .

Inspection of a large magnification image of a cracked region (Figure 3D and Figure S7A–F for additional images) shows that the MWNTs are covered with a PA sheath. In this region, dFMN-MWNT (Figure 3E) has a *ca.* 11 nm diameter and a thick and bumpy structure along its longitudinal direction. SEM images (Figure S8A,B) show that hot xylene-treated PA alone has a domain-like structure and that it does not exhibit a similar monoclinic pattern. This finding suggests that dFMN-MWNT induces crystallization of PA (see below). In addition, the results strongly support the conclusions that PA on MWNT has a higher solvent resistance and that it has different crystalline structure(s) than that of matrix PA not interacting with MWNTs, as color-coded in Figure 3A.

Confirmatory evidence for the existence of monoclinic PA on MWNT was gained by using high-resolution TEM

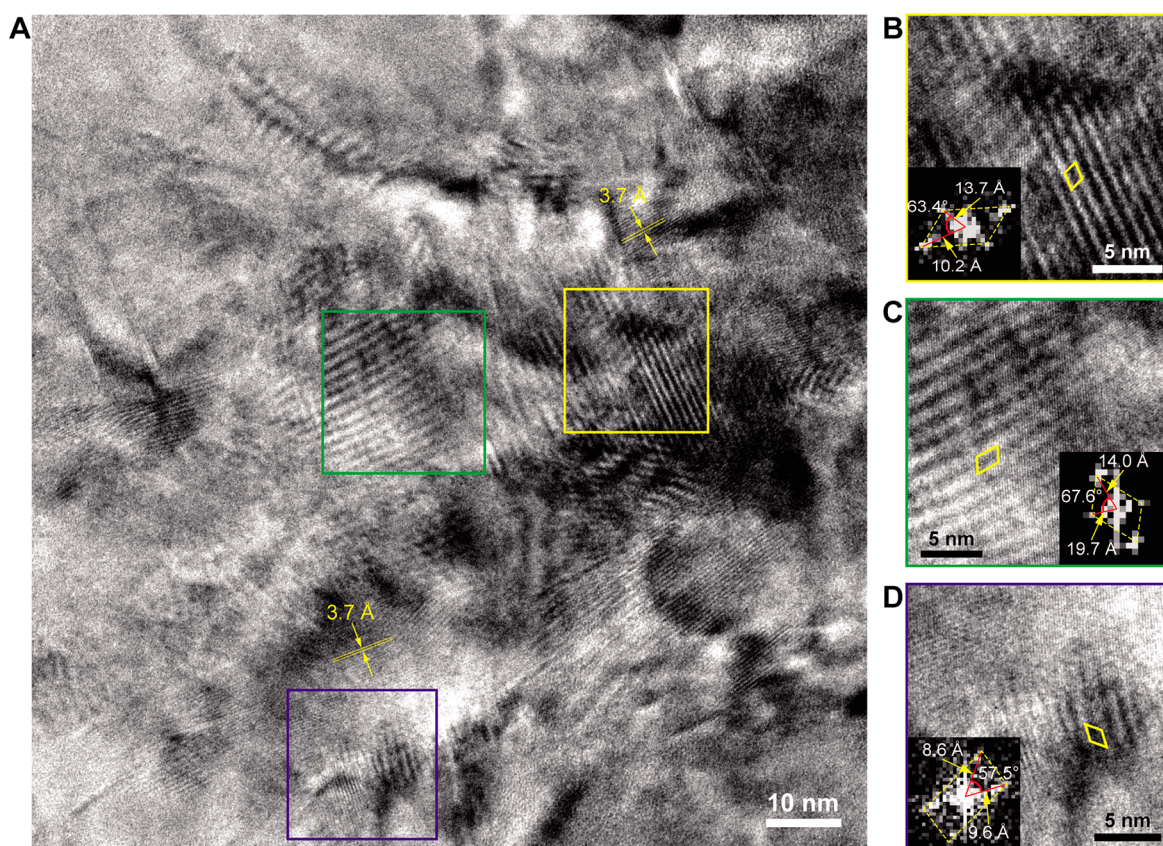


Figure 4. PA polymorph near MWNTs in PA-dFMN-MWNT-10. (A) HRTEM image of the surface of the nanocomposite dipped in hot *p*-xylene for 1 h. (B–D) Corresponding magnified HRTEM images of various polymorphs of PA near MWNTs corresponding to yellow, green, and blue squared regions of (A), respectively. Insets: FT image.

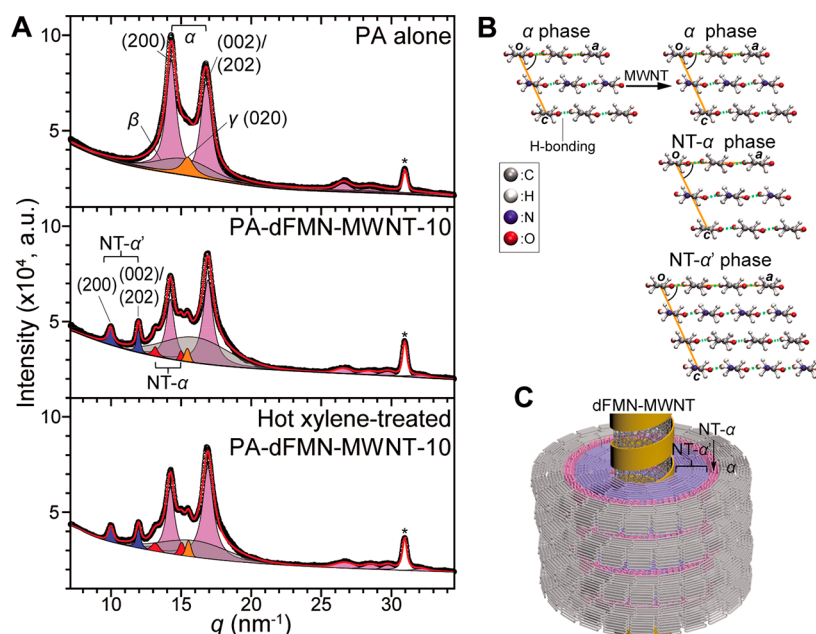


Figure 5. Polymorphism of nanocomposite PA-dFMN-MWNT-10. (A) GIXRD patterns of PA alone (top), PA-dFMN-MWNT-10 (middle), and hot xylene-treated PA-dFMN-MWNT-10 (bottom). Peaks have been deconvoluted by using color-coded Voigt fitting (pink, gray, orange, blue, and red colors denote reflections from α , mesomorphic β , γ , NT- α' , and NT- α , respectively). Peaks marked by an asterisk originate from a stainless-steel mount. (B) Top views of the α form of PA (left) and MWNT-derived α , NT- α , and NT- α' phases of PA-dFMN-MWNT-10 from top to bottom (right). (C) Schematics of PA polymorph around MWNT.

(HRTEM). An overnight exposure of a thin film of nanocomposite PA-dFMN-MWNT-10 to hot *p*-xylene vapor

(140 °C) resulted in microscopically swollen PA observed by HRTEM (data not shown). This observation encouraged us to

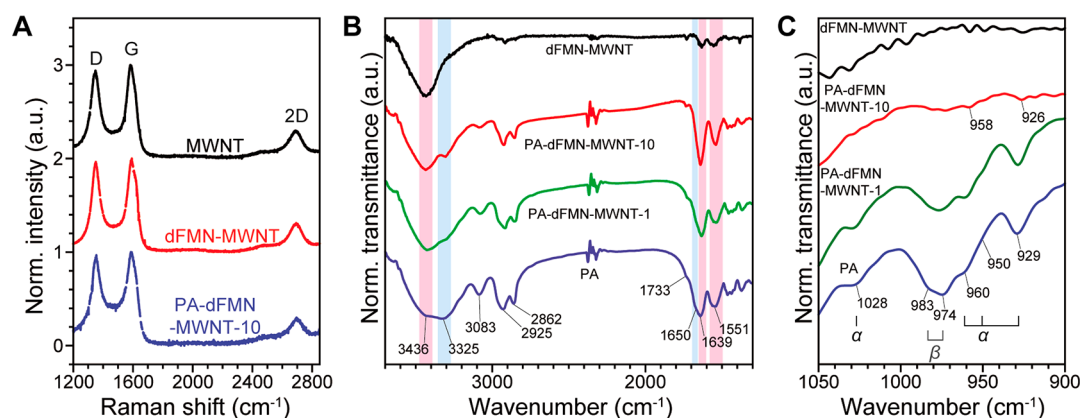


Figure 6. Raman and FT-IR spectra of nanocomposites. (A) Normalized Raman spectra of MWNT (black), dFMN-MWNT (red), PA-dFMN-MWNT-1 (green), and PA-dFMN-MWNT-10 (blue). Laser excitation: 532 nm. (B) Normalized FT-IR spectra of dFMN-MWNT (black), PA-dFMN-MWNT-10 (red), PA-dFMN-MWNT-1 (green), and PA (blue). Normalizations were conducted against the intensity of N–H stretch near 3436 cm^{-1} . Red and blue shades indicate increased and decreased band intensities, respectively, occurring upon addition of dFMN-MWNT. (C) The 900–1050 cm^{-1} range of the FT-IR spectra, which is related to the polymorph of PA.

conduct a TEM measurement on a sample prepared by immersion in *p*-xylene for 1 h (see [Methods](#)). Inspection of [Figure 4A](#), containing a HRTEM image of MWNT embedded in PA, shows that MWNT (arrow) has a wall spacing of 0.37 nm which is in accordance with that of MWNT⁴² and interestingly that monoclinic PA is present near MWNT (yellow box). As determined by using FT ([Figure 4B](#) and inset), the unit cell is monoclinic and has dimensions of *ca.* 13.7 Å × 10.2 Å with a contained angle of 63°. Similarly, other unit cells such as a doubled value of one segment of monoclinic unit (*i.e.*, 14.0 Å × 19.7 Å with contained angle of 67.6°) and smaller monoclinic unit cell (*i.e.*, 9.6 Å × 8.6 Å with contained angle of 57.5°) exist near MWNT. Other monoclinic polymorphs are also present ([Figure S9A–E](#)) with unit cells varying from 9.0 Å × 7.7 Å to 20.9 Å × 14.8 Å with respective contained angles of 56.3° to 83.7°. These observations demonstrate that a profound polymorph of PA occurs when it interacts with the dFMN-MWNTs.

By using grazing-incidence X-ray diffraction (GIXRD), we found that polymorphs of PA near MWNTs differ from those of PA alone. The top panel of [Figure 5A](#) shows the GIXRD pattern of PA alone. The deconvoluted diffraction pattern obtained by Voigt fitting shows that two main polymorphs (*i.e.*, α ⁶⁵ and γ ⁶⁶) of PA coexist. These are identified by the characteristic peaks at scattering vector $q = 14.30$ and 16.79 nm^{-1} (pink color), corresponding to respective (200) and (002)/(202) reflections of the α phase with monoclinic unit cell. In addition, another scattering vector occurs at $q = 15.48 \text{ nm}^{-1}$ (orange) that is associated with the (002) reflection of the γ phase (pseudohexagonal). PA undergoing H-bonding in a parallel chain arrangement of amide bonds causes the γ phase, whereas H-bonding in an antiparallel chain arrangement is responsible for the α form.^{65,66} Moreover, a broad diffraction peak is observed at $q = 15.21 \text{ nm}^{-1}$ which represents the mesomorphic (or semicrystalline) β form^{67,68} of PA that is associated with an H-bonded intermediate between the α and γ phases. Overall, owing to the presence of a more enhanced H-bonding, the α phase is the dominant and most stable crystalline phase at room temperature,⁶⁹ and it contributes to 74% based on the ratio of area of α phase over the areas of other crystalline and semicrystalline phases (see [Table S1](#)). The unit cell of the α phase (*i.e.*, $a = 9.71 \text{ Å}$, $c = 8.27 \text{ Å}$, $\beta = 64.8^\circ$) is monoclinic unit, which is in good agreement with the

results of a previous study (*i.e.*, $a = 9.56 \text{ Å}$, $c = 8.01 \text{ Å}$, $\beta = 67.5^\circ$).⁶⁵ The PA-dFMN-MWNT-10 contains two additional pairs of peaks at 9.96 and 11.95 nm^{-1} (blue) and 13.16 and 15.00 nm^{-1} (red) along with major characteristic peaks of PA at 14.23 and 16.91 nm^{-1} . Although the exact conformation of each polymorph is unknown, the results of calculation suggest that two pairs of peaks originate from a polymorph with monoclinic unit cells that have dimensions listed in [Table S2](#). Noticeably, as compared to that of PA alone, the α phase of PA-dFMN-MWNT-10 (right top of [Figure 5B](#)) is slightly compressed along the c axis (left side of [Figure 5B](#)). Moreover, the two additional polymorphs associated with PA-dFMN-MWNT-10 ([Figure 5A](#)) have much larger unit cells and are identified as previously unobserved MWNT-induced monoclinic NT- α' and NT- α phases (*i.e.*, $a = 13.88 \text{ Å}$, $c = 11.56 \text{ Å}$, $\beta = 65.4^\circ$ and $a = 10.62 \text{ Å}$, $c = 9.32 \text{ Å}$, $\beta = 64^\circ$, respectively). Especially, interesting is the fact that the HRTEM study shows similar monoclinic unit cells like NT- α' and PA in the presence of MWNT ([Figure 4B](#) for NT- α' and [Figure 4D](#) for PA only). Other unit cells observed in the HRTEM study are reasonable variations when consideration is given to the full width at half-maximum of the GIXRD peaks accounting for unit cell heterogeneity. Based on an analysis of the lattice parameters ([Table S2](#)), the main differences between polymorphs are the numbers of PA repeat units in the unit cells (*i.e.*, 18 vs 8, see [Figure 5B](#)) and the resulting packing densities (ρ). The calculated ρ values given in [Table S1](#), determined by assuming similar b values corresponding to two PA repeats (*i.e.*, 17.24 Å), suggest that the phase densities decrease in the order of NT- α' (*i.e.*, calculated $\rho = 1.35 \text{ g/cm}^3$), α , and NT- α . These results suggest the reason for the SEM observation that PA remains on the MWNTs after the solvent treatment.

The mesomorphic β phase significantly increases when the amount of MWNT in the nanocomposite increases and it is preferentially removed by hot xylene treatment. For instance, PA only contains a 19% β phase among crystalline and semicrystalline phases, while the contributions of β phases in PA-dFMN-MWNT-10 and its hot xylene-treated analog are 41% and 29%, respectively. The possibility that a phase transition from β to α is promoted by hot xylene treatment (*i.e.*, 100°C) was excluded because it is known that a phase transition of this type occurs at much higher temperatures (*i.e.*, 150°C).⁶⁸ The crystallinity content in the nanocomposite that

is associated with the presence of MWNT was also evaluated. The results show that PA-dFMN-MWNT-10 contains 5.7 and 2.8% of the NT- α' and NT- α phases, respectively, and similar phase contents are present in xylene-treated PA-dFMN-MWNT-10 (*i.e.*, 5.0% NT- α' and 3.5% NT- α). In addition, a decreased (200) reflection occurs in major α phase. This reduction originates from a disturbed arrangement of a H-bonded PA sheet on MWNT along the a axis (Figure 5B), which is observed in other PA nanocomposites containing fillers such as clay⁷⁰ and graphene oxide.⁷¹ Together with viewing the monoclinic MWNT structure in the FT image, the GIXRD result suggests that the networked MWNT structure originates from the α form of the PA matrix. This finding is important because it indicates that the hierarchical MWNT structure is induced by interactions between PA in the matrix and the PA on MWNT. Altogether with HRTEM and GIXRD experiments, these results suggest that hierarchical structure, as shown in Figure 5C in which dFMN-MWNT, is surrounded by monoclinic PA phases whose crystalline chain direction is perpendicular to the longitudinal axis of MWNT.

Another reason for the high σ values observed for the PA-dFMN-MWNT nanocomposites is the existence of low levels of defects in the MWNTs that form during their preparation. This can be seen by analyzing Raman spectra of MWNT (black), dFMN-MWNT (red), and PA-dFMN-MWNT-10 (blue) (Figure 6A), which contain D, G, and 2D bands at 1350, 1600, and 2700 cm^{-1} , respectively. The D, G, and 2D bands correspond to defective, graphitic bands, and overtones of D and G bands, respectively.⁷² The introduction of defects into the MWNT is known to cause an initial increase in the intensity of the D band at *ca.* 1350 cm^{-1} .⁷² We observed that compared to that of bare MWNT, the Raman spectra of dFMN-MWNT and PA-dFMN-MWNT-10 do not display significant increases in the intensities of the D band as compared to that of the G band, although slight increases in the full width at half-maximum of the D and G bands do take place. Moreover, the fact that the intensity ratio of the D and G bands, which reflects defect density,⁷² remains nearly the same (*i.e.*, 0.95) for all of the samples suggests that the ball milling and melt extrusion processes do not cause an introduction of a significant level of MWNT defects.

FT-infrared (FT-IR) spectroscopy was utilized to gain an understanding of H-bonded crystalline phases. In Figure 6B, normalized FT-IR spectra of PA (blue), PA-dFMN-MWNT-1 (green), PA-dFMN-MWNT-10 (red) and dFMN-MWNT (black) are shown. The spectrum of PA, which consists of amide and $(\text{CH}_2)_5$ moieties, contains signals at 3436, 3325, 1639, and 1551 cm^{-1} assigned to free N–H stretching, H-bonded N–H stretching, and amide I and II bands, respectively.⁷³ Also, strong asymmetric and symmetric C–H stretching bands are present at 2925 and 2862 cm^{-1} , respectively. Notably, upon increasing the wt % of dFMN-MWNT, the spectra of the PA-dFMN-MWNT nanocomposites exhibit increases in the intensity of free N–H stretching band (3436 cm^{-1}) and decreases in that of the H-bonded N–H stretching band (3325 cm^{-1}). In addition, the amide I band at 1639 cm^{-1} becomes sharper. Especially characteristic is that the intensity of the up-frequency shoulder of the amide I band at 1650 cm^{-1} , which is assigned to free amide I,⁷³ decreases significantly, whereas the H-bonded amide I band at 1639 cm^{-1} increases as the wt % of dFMN-MWNT in the nanocomposite increases. Finally, the intensity of the amide II band at 1551 cm^{-1} increases as well. The fact that the

spectrum of dFMN-MWNT contains free N–H stretching and amide I and II bands suggests that the isalloxazine ring remains on MWNT during the annealing process. Furthermore, the observations suggest that interchain H-bonding between PA is disrupted in association with structural changes taking place upon nanocomposite formation.

Analysis of the 900–1050 cm^{-1} range of FT-IR spectra (Figure 6C) provides information about the crystallization morphology of PA in the nanocomposites. Characteristic bands associated with the γ phase at 913 and 1003 cm^{-1} (ref 68) are absent in spectra of the composites. Except for the case of dFMN-MWNT (black), the spectra contain bands for the α phase^{68,74} at 929, 950, 961, and 1028 cm^{-1} , and for the β form^{68,74} at 974, 1074, and 1119 cm^{-1} . The near absence of bands corresponding to the γ phase is in excellent agreement with the GIXRD results. Moreover, slight down frequency shifts of several bands (926 and 958 cm^{-1}) occur in spectral regions associated with the phase α . Bands in this region originate from the normal mode of amide bending and/or angular deformation of the CH_2 unit. Quarti *et al.*⁷⁵ reported the results of theoretical calculations of the IR spectra for PA polymorphs which showed that the *ca.* 930 cm^{-1} band of the α phase originates from polymeric chain regularity, whereas others are a consequence of H-bonding mediated crystallinity. In addition, their observations demonstrated that IR bands associated with crystalline chains appear at a higher frequency than those corresponding to single chains. Thus, when combined with studies conducted earlier by Quarti *et al.*, the current results suggest that the presence of MWNTs in the nanocomposite causes a partial loss in the long-range regularity and chain crystallinity of the PA owing to a decrease in H-bonding.

We next assessed the effect of the presence of MWNT on the mechanical properties of PA in the nanocomposite by measuring tensile strengths. For this purpose, rectangular samples were loaded into an Instron instrument and subjected to stress–strain curve analysis. As shown in Figure S10A, PA alone has a tensile strength of 45 MPa, which matches typical values,^{76,77} and a decrease in tensile strength occurs upon increasing the wt % of MWNT in the nanocomposite reaching 12 MPa for PA-dFMN-MWNT-10, which is about 27% of PA alone. These results suggest that incorporation of dFMN-MWNT decreases the mechanical strength of the nanocomposite. The low mechanical strength might originate from the aforementioned microcrack and microvoid (Figure S10B) as well as weakened H-bonding of PA owing to the observed polymorph. Improving the density of the nanocomposite is underway by modifying a hot press which is a topic of future research.

Role of FMN. Polymorphism of PA in the PA-dFMN-MWNTs nanocomposites leads to questions about the role played by the *N*-pentadienyl side chains present in the dFMN-MWNT components. Notably, a composite prepared from PA and MWNT in the absence of interfacing surfactant under similar conditions does not have any MWNT-related polymorphs.^{31,64} This finding suggests that dFMN plays an important role in polymorph formation. This effect might be a consequence of the hydrophobic nature of the *N*-pentadienyl side chain, along with the H-bonding capable uracil moiety of dFMN. To assess this proposal, we estimated the solubility parameter δ of *N*-pentadienyl side chain by using the equation $\delta = \sqrt{E_{\text{coh}}/V}$, where E_{coh} and V denote the cohesive energy (J/

mol) and molar volume (cm^3/mol), respectively.⁷⁸ Using this method, the δ of the pentadienyl moiety in dFMN-MWNT is estimated to be $15.8 \text{ J}^{1/2}/\text{cm}^{3/2}$ which is close to that of PA (i.e., $25.4 \text{ J}^{1/2}/\text{cm}^{3/2}$).⁷⁸ Thus, it appears that the dFMN component of dFMN-MWNT in the nanocomposites could enable a high level of miscibility of dFMN-MWNT with the PA, which would induce the formation of MWNT-derived α phases. In addition, the similarities between their crystallinities could lead to an organization of MWNTs into a monoclinic pattern, resulting in higher σ . Although the aforementioned δ can be a reason for interfacial miscibility between PA and MWNT, it would be difficult to explain different polymorphs of PA on MWNT. We speculate that H-bonding between isalloxazine and the PA chain might occur and be a reason. It is noteworthy that helix of FMN on carbon nanotube is maintained by the tilted quadruple H-bonding mentioned earlier. H-bonding between uracil moieties and amide groups of PA might occur and serve as the nucleation center for the NT- α' phase. Such a H-bonding configuration prompts PA main chains packed along the transverse direction of MWNT, as shown in Figure 5C.

CONCLUSIONS

As described above, we developed a method to produce a highly electrically conductive PA nanocomposite with a monoclinic MWNT network structure using chemically transformable FMN. In the process, FMN serves as a surfactant for formation of the conjugate FMN-MWNT in which MWNTs are individualized through isalloxazine-promoted wrapping and phosphate-induced repulsive interactions. Thermal activation of FMN-MWNT then leads to the production of dFMN-MWNT, in which the ribityl phosphate chain of FMN is transformed into a corresponding *N*-pentadienyl side chain. The presence of the hydrophobic *N*-pentadienyl moiety in the dFMN component prompts the formation of crystallinity regions in PA in the PA-dFMN-MWNT composite. The σ of PA-dFMN-MWNT containing 10 wt % of dFMN-MWNT is 100 S/m, the highest value reported thus far for polymer nanocomposites with MWNT. Studies using composites subjected to solvent-assisted partial dissolution of PA matrix reveal that MWNT has three-dimensional monoclinic network structure in the polymer matrix. XRD results indicate that PA in the nanocomposite has a monoclinic α phase as its major crystalline form, and the presence of dFMN-MWNT induces monoclinic PA formation on the surface of MWNT. The morphological interlocking induces the formation of a monoclinic MWNT network structure. In addition, the enhanced σ of the nanocomposite results from a preservation of the structural integrity of the MWNT along with low defect formation during multistep fabrication processes. However, an increase in the wt % of MWNT in the PA-dFMN-MWNT results in the production of MWNT-related polymorphs and lowers the amide H-bonding interactions in PA. The observations made in this effort demonstrate that the noncovalent method employing MWNT is a viable strategy to prepare high-performance nanocomposites. In terms of cost effectiveness, compared to PA and MWNT (1.6 and 42 \$/kg), FMN is an expensive substance (i.e., 2.9 \$/g). However, FMN accounts for only ca. 2 wt % in PA-dFMN-MWNT-10 and is reclaimed in the developed process by up to 50% during the filtration step. A tunneling-dominant percolated MWNT network structure can be utilized as a material with negative permittivity.⁷⁹ Thus, the

observations made in this investigation have the potential of stimulating the development of FMN-based nanocomposites that have a tunable electrical conductance and useful high-end electronic applications.

METHODS

Materials and Instrumentation. MWNT (diameter: ca. 11 nm, length: <40 nm, wall number: 10–15 layers) was kindly donated by LG Chem (Daejun, Republic of Korea).⁴² The monosodium salt form of FMN with a purity >93% was purchased from TCI (Seoul, Republic of Korea). PA was obtained from Hyosung Chemicals (relative viscosity: 2.53 in conc. H_2SO_4 at 475 °C, cat. no.: 1011 BRT, Republic of Korea). Deionized (DI) water whose electrical resistance is >18 M Ω was utilized in all experiments. Raman spectra were acquired by using a custom-made setup⁸⁰ with a 532 nm laser with 1 mW power via a backscattering geometry and were calibrated using the Si peak (520.89 cm^{-1}) as an internal reference. SEM images were acquired by using field emission SEMs (SU8000, Hitachi or 7610F-plus, JEOL Ltd., Japan) operating at 5 kV as an acceleration voltage. For SEM image for partially dissolved sample, *p*-xylene was treated for 1 h at 100 °C. OM images were obtained by using reflection (BX51, Olympus, Japan) or transmission (BX41, Olympus, Japan) modes with a CMOS camera. Mechanical strengths were obtained using an Instron 3343 (Illinois Tool Works Inc., IL, USA) with a 1 kN load cell.

Noncovalent Functionalization of MWNT with FMN and Annealing. The dispersion process was carried out using a previously described procedure.⁴² An aqueous dispersion of MWNT and FMN was subjected to either vibrational ball milling (vibrational frequency: 50 Hz, Pulverisette 23, Fritsch, Germany) or a rotational ball milling (PL-BMSL, Punglim, Seoul, Republic of Korea) for small and large quantities, respectively. Briefly, a mixture of 10.0 g of MWNT and 8.0 g of FMN in 300 mL of water was milled for 1 h using 2 vol % of zirconia balls (diameter = 5 mm). The resulting black slurry was vacuum-filtered by using a Buchner funnel and a water-circulated aspirator (Eyela A-3S, USA). The obtained black FMN-MWNT solid was washed with DI water several times to remove and reclaim unbound FMN and subjected to lyophilization to produce a dry FMN-MWNT as a powder. dFMN-MWNT containing *N*-pentadienyl isalloxazine was obtained by annealing the FMN-MWNT powder at 450 °C under air for 2 h in a conventional quartz tubular reactor. The average MWNT length produced by this process is ca. 700 nm.⁴²

Compounding and Specimen Preparation. PA-dFMN-MWNT nanocomposites comprised of PA and varying amounts of dFMN-MWNT were prepared using a co-rotating twin-screw melt extruder (LME-230, Dynisco Instruments, MA, USA) at a barrel temperature of $250 \text{ }^\circ\text{C} \pm 5 \text{ }^\circ\text{C}$ with a screw speed of 60 rpm to produce PA-dFMN-MWNT-1, -3, -5 and -10, using 1, 3, 5, and 10 wt % of dFMN-MWNT, respectively. The final specimens were prepared as thin films (i.e., 90–405 μm thickness) using a hot press machine (Carver Inc., IN, USA) operating at 250 °C during both preheating and compression processes, followed by cooling to 40 °C.

Electrical Measurements. The σ of PA-dFMN-MWNT nanocomposites was obtained by using a four point probe with interpin distance of 5 mm (MCP-TP03P, Mitsubishi Chemical Analytech., Japan) and was averaged from three separate positions. Then, σ was obtained from the measured thickness of the melt-pressed composite sheet. Anisotropic σ measurements were conducted by a two probe method in which vertical and horizontal σ were measured by controlling the distance of the probes with a micrometer.

AFM Measurements. Height topographies were acquired by using a commercially available AFM (NX10, Park systems, Republic of Korea). An Al-coated silicon cantilever with a spring constant 37 N/m, a resonance frequency of 300 kHz, and quoted radius of ca. 6 nm (ACTA, App Nano, CA, USA) were utilized. Typically, a 512×512 pixel image was collected. To measure height images of dFMN-MWNT, as-prepared dFMN-MWNT powder was redispersed in *N,N'*-dimethylformamide (DMF) with a brief bath sonication (1510 sonicator, 70 W, Branson, CT, USA). Dispersed dFMN-MWNT was

deposited on 285 nm-thick SiO₂/Si substrates by dipping for 10 min. Then, the substrate was rinsed with fresh DMF several times and dried under a N₂ stream.

TGA Measurements. Thermal properties were determined mainly by using a simultaneous thermal analyzer (STA 409 PC, Netzsch-Gerätebau GmbH, Germany). For this purpose, ca. 25 mg of FMN, dFMN, MWNT, and dFMN-MWNT were placed on alumina pans. A typical scanning range was from 30 to 900 °C with a ramping rate of 10 °C/min with a 100 standard cubic centimeter per min flow of synthetic air composed of 21 vol % O₂ in N₂ unless otherwise noted. Preactivation of MWNT was conducted at 450 °C for 1 h under an air atmosphere.

GIXRD Measurements. GIXRD patterns were obtained using a high-resolution X-ray diffractometer (SmartLab, Rigaku, Japan) with a Cu K_α radiation ($\lambda = 1.541 \text{ \AA}$) and a scan speed of 2°/min. The samples were placed onto a notched stainless-steel mount with a fixed incident angle (0.5°) with respect to the X-ray source.

HRTEM Measurement. HRTEM measurements were made by using a Tecnai G² F30ST (FEI company, OR, USA) operating at 300 kV acceleration voltage. Initially, the PA-dFMN-MWNT-10 sample was ground by using 120-grit sandpaper. Raman and optical microscopy measurements confirm that the collected ground debris up to a few hundred micrometers contains sample only. The resulting debris was spread on a copper TEM grid covered with an ultrathin carbon support (LC200-Cu, lot no.: 110727, 200 mesh, Ted Pella, CA, USA). In sample 1, the TEM grid was exposed to a hot vapor of *p*-xylene overnight. In sample 2, which was a successful case, the TEM grid was immersed in a 100 °C *p*-xylene for 1 h. Optionally, samples were negatively stained by using 2 wt % H₃PO₄·12WO₃·xH₂O (Acros Organics, USA) in 2 wt % of benzyl alcohol in water.

Lattice Visualization. The initial α form of PA was constructed by adaptation of a crystal structure from the literature.⁶⁵ A monoclinic unit cell (P2₁) with determined dimension (Table S2) was utilized to construct α and NT- α . In the case of NT- α , additional PA chains along the *a* and *c* axes were introduced for construction of an enlarged unit cell. Lattice visualization was performed with VMD 1.9.3 (ref 81).

ASSOCIATED CONTENT

Supporting Information

The Supporting Information is available free of charge at <https://pubs.acs.org/doi/10.1021/acsnano.0c05170>.

AFM height images of dFMN-MWNT (Figure S1), plots of TGAs and corresponding derivatives of weight (Figure S2), surface morphologies of nanocomposites (Figure S3), OM images of pristine PA and xylene-treated PA (Figure S4), SEM images of as-prepared dFMN-MWNT (Figure S5), monoclinic arrangement of MWNT in PA-dFMN-MWNT-10 (Figure S6), SEM images of MWNT near microcracks in PA-dFMN-MWNT-10 (Figure S7), SEM images of PA under similar treatment (Figure S8), HRTEM images and FT images of various polymorphs of PA (Figure S9), and tensile strengths of PA only and nanocomposites (Figure S10). Scattering vector, crystal density, and crystalline fraction from GIXRD data (Table S1) and determined lattice parameters with minimum errors (Table S2) (PDF)

AUTHOR INFORMATION

Corresponding Authors

No-Hyung Park — Department of Textile Convergence of Biotechnology and Nanotechnology, Korea Institute of Industrial Technology, Ansan-Si, Gyeonggi-Do 15588, Republic of Korea; Email: nohyung@kitech.re.kr

Sang-Yong Ju — Department of Chemistry, Yonsei University, Seoul 03722, Republic of Korea; orcid.org/0000-0002-6939-5296; Email: syju@yonsei.ac.kr

Authors

Minsuk Park — Department of Chemistry, Yonsei University, Seoul 03722, Republic of Korea; orcid.org/0000-0002-1522-6403

Seulki Yoon — Human Convergence Technology Group, Korea Institute of Industrial Technology, Ansan-Si, Gyeonggi-Do 15588, Republic of Korea

Junmo Park — Department of Chemistry, Yonsei University, Seoul 03722, Republic of Korea; orcid.org/0000-0003-4217-9056

Complete contact information is available at: <https://pubs.acs.org/doi/10.1021/acsnano.0c05170>

Author Contributions

S.J. conceived the idea and wrote the manuscript. M.P. with the help of J.P. prepared dFMN-MWNT samples. S.Y. and N.P. prepared the nanocomposite and characterized the electrical properties. M.P. characterized the nanocomposite by using AFM, GIXRD, HRTEM, Raman, and FTIR measurements.

Notes

The authors declare the following competing financial interest(s): This work was provisionally filed in patent office, Republic of Korea (application number: 10-2019-0059257, May 21, 2019, Republic of Korea).

ACKNOWLEDGMENTS

This research was mainly supported by the Basic Science Research Program through the National Research Foundation of Korea (NRF) funded by the Ministry of Education, Science, and Technology (2019R1F1A1061624, 2020R1F1A1076983, 2020R1A4A1017737, and in part 2019R1A6A3A13091240). This research was also partially supported by the Korea Basic Science Institute under the R&D program (project no. D39701) supervised by the Ministry of Science and ICT.

REFERENCES

- (1) Iijima, S. Helical Microtubules of Graphitic Carbon. *Nature* **1991**, *354*, 56–58.
- (2) Gupta, T. K.; Singh, B. P.; Mathur, R. B.; Dhakate, S. R. Multi-Walled Carbon Nanotube–Graphene–Polyaniline Multiphase Nanocomposite with Superior Electromagnetic Shielding Effectiveness. *Nanoscale* **2014**, *6*, 842–851.
- (3) Wang, C.; Murugadoss, V.; Kong, J.; He, Z.; Mai, X.; Shao, Q.; Chen, Y.; Guo, L.; Liu, C.; Angaiah, S.; Guo, Z. Overview of Carbon Nanostructures and Nanocomposites for Electromagnetic Wave Shielding. *Carbon* **2018**, *140*, 696–733.
- (4) Lyu, L.; Liu, J.; Liu, H.; Liu, C.; Lu, Y.; Sun, K.; Fan, R.; Wang, N.; Lu, N.; Guo, Z.; Wujcik, E. K. An Overview of Electrically Conductive Polymer Nanocomposites toward Electromagnetic Interference Shielding. *Eng. Sci.* **2018**, *2*, 26–42.
- (5) Zhang, D.; Sun, J.; Lee, L. J.; Castro, J. M. Overview of Ultrasonic Assisted Manufacturing Multifunctional Carbon Nanotube Nanopaper Based Polymer Nanocomposites. *Eng. Sci.* **2020**, *10*, 35–50.
- (6) Yan, X.; Liu, J.; Khan, M. A.; Sheriff, S.; Vupputuri, S.; Das, R.; Sun, L.; Young, D. P.; Guo, Z. Efficient Solvent-Free Microwave Irradiation Synthesis of Highly Conductive Polypropylene Nanocomposites with Lowly Loaded Carbon Nanotubes. *ES Mater. Manuf.* **2020**. DOI: [10.30919/esmm5f716](https://doi.org/10.30919/esmm5f716)

- (7) Wu, M.; Ge, S.; Jiao, C.; Yan, Z.; Jiang, H.; Zhu, Y.; Dong, B.; Dong, M.; Guo, Z. Improving Electrical, Mechanical, Thermal and Hydrophobic Properties of Waterborne Acrylic Resin-Glycidyl Methacrylate (GMA) by Adding Multi-Walled Carbon Nanotubes. *Polymer* **2020**, *200*, 122547.
- (8) Park, C.; Ounaies, Z.; Watson, K. A.; Crooks, R. E.; Smith, J.; Lowther, S. E.; Connell, J. W.; Siochi, E. J.; Harrison, J. S.; Clair, T. L. S. Dispersion of Single Wall Carbon Nanotubes by *In Situ* Polymerization under Sonication. *Chem. Phys. Lett.* **2002**, *364*, 303–308.
- (9) Park, M.; Kim, H.; Youngblood, J. P. Strain-Dependent Electrical Resistance of Multi-Walled Carbon Nanotube/Polymer Composite Films. *Nanotechnology* **2008**, *19*, 055705.
- (10) Wei, H.; Wang, H.; Li, A.; Cui, D.; Zhao, Z.; Chu, L.; Wei, X.; Wang, L.; Pan, D.; Fan, J.; Li, Y.; Zhang, J.; Liu, C.; Wei, S.; Guo, Z. Multifunctions of Polymer Nanocomposites: Environmental Remediation, Electromagnetic Interference Shielding, and Sensing Applications. *ChemNanoMat* **2020**, *6*, 174–184.
- (11) Chen, J.; Yu, Q.; Cui, X.; Dong, M.; Zhang, J.; Wang, C.; Fan, J.; Zhu, Y.; Guo, Z. An Overview of Stretchable Strain Sensors from Conductive Polymer Nanocomposites. *J. Mater. Chem. C* **2019**, *7*, 11710–11730.
- (12) Grady, B. P. Recent Developments Concerning the Dispersion of Carbon Nanotubes in Polymers. *Macromol. Rapid Commun.* **2010**, *31*, 247–257.
- (13) Chen, J.; Liu, B.; Gao, X.; Xu, D. A Review of the Interfacial Characteristics of Polymer Nanocomposites Containing Carbon Nanotubes. *RSC Adv.* **2018**, *8*, 28048–28085.
- (14) McNally, T.; Pötschke, P. *Polymer–Carbon Nanotube Composites*, 1st ed.; Woodhead Publishing: Cambridge, 2011; p 848.
- (15) Ke, G.; Guan, W.; Tang, C.; Guan, W.; Zeng, D.; Deng, F. Covalent Functionalization of Multiwalled Carbon Nanotubes with a Low Molecular Weight Chitosan. *Biomacromolecules* **2007**, *8*, 322–326.
- (16) Sakellariou, G.; Ji, H.; Mays, J. W.; Hadjichristidis, N.; Baskaran, D. Controlled Covalent Functionalization of Multiwalled Carbon Nanotubes Using [4 + 2] Cycloaddition of Benzocyclobutenes. *Chem. Mater.* **2007**, *19*, 6370–6372.
- (17) Chen, Y.; Tao, J.; Li, S.; Khashab, N. M. Compositing Polyetherimide with Polyfluorene Wrapped Carbon Nanotubes for Enhanced Interfacial Interaction and Conductivity. *ACS Appl. Mater. Interfaces* **2014**, *6*, 9013–9022.
- (18) Liu, R.; Chen, Y.; Ma, Q.; Luo, J.; Wei, W.; Liu, X. Noncovalent Functionalization of Carbon Nanotube Using Poly(vinylcarbazole)-Based Compatibilizer for Reinforcement and Conductivity Improvement in Epoxy Composite. *J. Appl. Polym. Sci.* **2017**, *134*, 45022.
- (19) Cadek, M.; Coleman, J. N.; Ryan, K. P.; Nicolosi, V.; Bister, G.; Fonseca, A.; Nagy, J. B.; Szostak, K.; Béguin, F.; Blau, W. J. Reinforcement of Polymers with Carbon Nanotubes: The Role of Nanotube Surface Area. *Nano Lett.* **2004**, *4*, 353–356.
- (20) Odian, G. *Principles of Polymerization*, 4th ed.; John Wiley & Sons, Inc.: New York, 1991; pp 102–104.
- (21) Lingesh, B. V.; Ravi Kumar, B. N.; Rudresh, B. M.; Reddappa, H. N. Hybridization Effect of Fibers on Mechanical Properties of PA66/PP Blend-Based Thermoplastic Composites. *Adv. Compos. Hybrid Mater.* **2018**, *1*, 766–776.
- (22) Rudresh, B. M.; Ravi Kumar, B. N.; Madhu, D. Combined Effect of Micro- and Nano-Fillers on Mechanical, Thermal, and Morphological Behavior of Glass–Carbon PA66/PTFE Hybrid Nano-Composites. *Adv. Compos. Hybrid Mater.* **2019**, *2*, 176–188.
- (23) Sun, H.; Fang, Z.; Li, T.; Lei, F.; Jiang, F.; Li, D.; Zhou, Y.; Sun, D. Enhanced Mechanical and Tribological Performance of PA66 Nanocomposites Containing 2D Layered α -Zirconium Phosphate Nanoplatelets with Different Sizes. *Adv. Compos. Hybrid Mater.* **2019**, *2*, 407–422.
- (24) Liu, Y.; Kumar, S. Polymer/Carbon Nanotube Nano Composite Fibers—A Review. *ACS Appl. Mater. Interfaces* **2014**, *6*, 6069–6087.
- (25) Naskar, A. K.; Keum, J. K.; Boeman, R. G. Polymer Matrix Nanocomposites for Automotive Structural Components. *Nat. Nanotechnol.* **2016**, *11*, 1026–1030.
- (26) Zou, J.; Liu, J.; Karakoti, A. S.; Kumar, A.; Joung, D.; Li, Q.; Khondaker, S. I.; Seal, S.; Zhai, L. Ultralight Multiwalled Carbon Nanotube Aerogel. *ACS Nano* **2010**, *4*, 7293–7302.
- (27) Tang, C.; Long, G.; Hu, X.; Wong, K.-w.; Lau, W.-m.; Fan, M.; Mei, J.; Xu, T.; Wang, B.; Hui, D. Conductive Polymer Nanocomposites with Hierarchical Multi-Scale Structures via Self-Assembly of Carbon-Nanotubes on Graphene on Polymer-Microspheres. *Nanoscale* **2014**, *6*, 7877–7888.
- (28) Li, Y.; Zhou, B.; Zheng, G.; Liu, X.; Li, T.; Yan, C.; Cheng, C.; Dai, K.; Liu, C.; Shen, C.; Guo, Z. Continuously Prepared Highly Conductive and Stretchable SWNT/MWNT Synergistically Composed Electrospun Thermoplastic Polyurethane Yarns for Wearable Sensing. *J. Mater. Chem. C* **2018**, *6*, 2258–2269.
- (29) Bekyarova, E.; Thostenson, E. T.; Yu, A.; Kim, H.; Gao, J.; Tang, J.; Hahn, H. T.; Chou, T. W.; Itkis, M. E.; Haddon, R. C. Multiscale Carbon Nanotube–Carbon Fiber Reinforcement for Advanced Epoxy Composites. *Langmuir* **2007**, *23*, 3970–3974.
- (30) Pötschke, P.; Fornes, T. D.; Paul, D. R. Rheological Behavior of Multiwalled Carbon Nanotube/Polycarbonate Composites. *Polymer* **2002**, *43*, 3247–3255.
- (31) Meincke, O.; Kaempfer, D.; Weickmann, H.; Friedrich, C.; Vathauer, M.; Warth, H. Mechanical Properties and Electrical Conductivity of Carbon-Nanotube Filled Polyamide-6 and Its Blends with Acrylonitrile/Butadiene/Styrene. *Polymer* **2004**, *45*, 739–748.
- (32) Chen, W.; Tao, X.; Liu, Y. Carbon Nanotube-Reinforced Polyurethane Composite Fibers. *Compos. Sci. Technol.* **2006**, *66*, 3029–3034.
- (33) Li, L.; Li, C. Y.; Ni, C. Polymer Crystallization-Driven, Periodic Patterning on Carbon Nanotubes. *J. Am. Chem. Soc.* **2006**, *128*, 1692–1699.
- (34) Li, L.; Li, B.; Hood, M. A.; Li, C. Y. Carbon Nanotube Induced Polymer Crystallization: The Formation of Nanohybrid Shish–Kebabs. *Polymer* **2009**, *50*, 953–965.
- (35) Li, B.; Li, L.; Wang, B.; Li, C. Y. Alternating Patterns on Single-Walled Carbon Nanotubes. *Nat. Nanotechnol.* **2009**, *4*, 358–362.
- (36) Massey, V. The Chemical and Biological Versatility of Riboflavin. *Biochem. Soc. Trans.* **2000**, *28*, 283–296.
- (37) Ju, S. Y.; Papadimitrakopoulos, F. Synthesis and Redox Behavior of Flavin Mononucleotide-Functionalized Single-Walled Carbon Nanotubes. *J. Am. Chem. Soc.* **2008**, *130*, 655–664.
- (38) Oh, H.; Sim, J.; Ju, S.-Y. Binding Affinities and Thermodynamics of Noncovalent Functionalization of Carbon Nanotubes with Surfactants. *Langmuir* **2013**, *29*, 11154–11162.
- (39) Park, M.; Park, J.; Lee, J.; Ju, S.-Y. Scaling of Binding Affinities and Cooperativities of Surfactants on Carbon Nanotubes. *Carbon* **2018**, *139*, 427–436.
- (40) Ju, S.-Y.; Doll, J.; Sharma, I.; Papadimitrakopoulos, F. Selection of Carbon Nanotubes with Specific Chiralities Using Helical Assemblies of Flavin Mononucleotide. *Nat. Nanotechnol.* **2008**, *3*, 356–362.
- (41) Ju, S.-Y.; Kopcha, W. P.; Papadimitrakopoulos, F. Brightly Fluorescent Single-Walled Carbon Nanotubes via an Oxygen-Excluding Surfactant Organization. *Science* **2009**, *323*, 1319–1323.
- (42) Kim, S.; Jang, M.; Park, M.; Park, N.-H.; Ju, S.-Y. A Self-Assembled Flavin Protective Coating Enhances the Oxidative Thermal Stability of Multi-Walled Carbon Nanotubes. *Carbon* **2017**, *117*, 220–227.
- (43) Yoon, W.; Lee, Y.; Jang, H.; Jang, M.; Kim, J. S.; Lee, H. S.; Im, S.; Boo, D. W.; Park, J.; Ju, S.-Y. Graphene Nanoribbons Formed by a Sonochemical Graphene Unzipping Using Flavin Mononucleotide as a Template. *Carbon* **2015**, *81*, 629–638.
- (44) Ayán-Varela, M.; Paredes, J. I.; Guardia, L.; Villar-Rodil, S.; Munuera, J. M.; Díaz-González, M.; Fernández-Sánchez, C.; Martínez-Alonso, A.; Tascón, J. M. D. Achieving Extremely Concentrated Aqueous Dispersions of Graphene Flakes and Catalytically Efficient Graphene-Metal Nanoparticle Hybrids with Flavin

Mononucleotide as a High-Performance Stabilizer. *ACS Appl. Mater. Interfaces* **2015**, *7*, 10293–10307.

(45) Gao, Z.; Zhi, C.; Bando, Y.; Golberg, D.; Serizawa, T. Noncovalent Functionalization of Disentangled Boron Nitride Nanotubes with Flavin Mononucleotides for Strong and Stable Visible-Light Emission in Aqueous Solution. *ACS Appl. Mater. Interfaces* **2011**, *3*, 627–632.

(46) Nakashima, N.; Fukuzawa, M.; Nishimura, K.; Fujigaya, T.; Kato, Y.; Staykov, A. Supramolecular Chemistry-Based One-Pot High-Efficiency Separation of Solubilizer-Free Pure Semiconducting Single-Walled Carbon Nanotubes: Molecular Strategy and Mechanism. *J. Am. Chem. Soc.* **2020**, *142*, 11847–11856.

(47) Ju, S.-Y.; Abanulo, D. C.; Badalucco, C. A.; Gascón, J. A.; Papadimitrakopoulos, F. Handedness Enantioselection of Carbon Nanotubes Using Helical Assemblies of Flavin Mononucleotide. *J. Am. Chem. Soc.* **2012**, *134*, 13196–13199.

(48) Sim, J.; Kim, S.; Jang, M.; Park, M.; Oh, H.; Ju, S.-Y. Determination of the Absolute Enantiomeric Excess of the Carbon Nanotube Ensemble by Symmetry Breaking Using the Optical Titration Method. *Langmuir* **2017**, *33*, 11000–11009.

(49) Wei, X.; Tanaka, T.; Hirakawa, T.; Yomogida, Y.; Kataura, H. Determination of Enantiomeric Purity of Single-Wall Carbon Nanotubes Using Flavin Mononucleotide. *J. Am. Chem. Soc.* **2017**, *139*, 16068–16071.

(50) Park, M.; Kim, S.; Kwon, H.; Hong, S.; Im, S.; Ju, S.-Y. Selective Dispersion of Highly Pure Large-Diameter Semiconducting Carbon Nanotubes by a Flavin for Thin-Film Transistors. *ACS Appl. Mater. Interfaces* **2016**, *8*, 23270–23280.

(51) Choi, D. S.; Ni, Y.; Fernández-Fueyo, E.; Lee, M.; Hollmann, F.; Park, C. B. Photoelectroenzymatic Oxyfunctionalization on Flavin-Hybridized Carbon Nanotube Electrode Platform. *ACS Catal.* **2017**, *7*, 1563–1567.

(52) Son, E. J.; Lee, S. H.; Kuk, S. K.; Pesic, M.; Choi, D. S.; Ko, J. W.; Kim, K.; Hollmann, F.; Park, C. B. Carbon Nanotube–Graphitic Carbon Nitride Hybrid Films for Flavoenzyme-Catalyzed Photoelectrochemical Cells. *Adv. Funct. Mater.* **2018**, *28*, 1705232.

(53) Huang, W.; Toshimitsu, F.; Ozono, K.; Matsumoto, M.; Borah, A.; Motoishi, Y.; Park, K. H.; Jang, J. W.; Fujigaya, T. Thermoelectric Properties of Dispersant-Free Semiconducting Single-Walled Carbon Nanotubes Sorted by a Flavin Extraction Method. *Chem. Commun.* **2019**, *55*, 2636–2639.

(54) Masłowska, J.; Malicka, M. Thermal Behaviour of Riboflavin. *J. Therm. Anal.* **1988**, *34*, 3–9.

(55) Kodgire, P. V.; Bhattacharyya, A. R.; Bose, S.; Gupta, N.; Kulkarni, A. R.; Misra, A. Control of Multiwall Carbon Nanotubes Dispersion in Polyamide 6 Matrix: An Assessment Through Electrical Conductivity. *Chem. Phys. Lett.* **2006**, *432*, 480–485.

(56) Bose, S.; Bhattacharyya, A. R.; Bondre, A. P.; Kulkarni, A. R.; Pötschke, P. Rheology, Electrical Conductivity, and the Phase Behavior of Cocontinuous PA6/ABS Blends with MWNT: Correlating the Aspect Ratio of MWNT with the Percolation Threshold. *J. Polym. Sci., Part B: Polym. Phys.* **2008**, *46*, 1619–1631.

(57) Ma, P.-C.; Liu, M.-Y.; Zhang, H.; Wang, S.-Q.; Wang, R.; Wang, K.; Wong, Y.-K.; Tang, B.-Z.; Hong, S.-H.; Paik, K.-W.; Kim, J.-K. Enhanced Electrical Conductivity of Nanocomposites Containing Hybrid Fillers of Carbon Nanotubes and Carbon Black. *ACS Appl. Mater. Interfaces* **2009**, *1*, 1090–1096.

(58) Zeng, X.; Xu, X.; Shenai, P. M.; Kovalev, E.; Baudot, C.; Mathews, N.; Zhao, Y. Characteristics of the Electrical Percolation in Carbon Nanotubes/Polymer Nanocomposites. *J. Phys. Chem. C* **2011**, *115*, 21685–21690.

(59) Sohi, N. J. S.; Bhadra, S.; Khastgir, D. The Effect of Different Carbon Fillers on the Electrical Conductivity of Ethylene Vinyl Acetate Copolymer-Based Composites and the Applicability of Different Conductivity Models. *Carbon* **2011**, *49*, 1349–1361.

(60) Alig, I.; Skipa, T.; Engel, M.; Lellinger, D.; Pegel, S.; Pötschke, P. Electrical Conductivity Recovery in Carbon Nanotube–Polymer Composites after Transient Shear. *Phys. Status Solidi B* **2007**, *244*, 4223–4226.

(61) Deng, H.; Bilotti, E.; Zhang, R.; Loos, J.; Peijs, T. Effect of Thermal Annealing on the Electrical Conductivity of High-Strength Bicomponent Polymer Tapes Containing Carbon Nanofillers. *Synth. Met.* **2010**, *160*, 337–344.

(62) Shang, S.; Zeng, W.; Tao, X.-m. High Stretchable MWNTs/Polyurethane Conductive Nanocomposites. *J. Mater. Chem.* **2011**, *21*, 7274–7280.

(63) John, S. Strong Localization of Photons in Certain Disordered Dielectric Superlattices. *Phys. Rev. Lett.* **1987**, *58*, 2486–2489.

(64) Kazemi, Y.; Kakroodi, A. R.; Mark, L. H.; Filletter, T.; Park, C. B. Effects of Polymer-Filler Interactions on Controlling the Conductive Network Formation in Polyamide 6/Multi-Walled Carbon Nanotube Composites. *Polymer* **2019**, *178*, 121684.

(65) Holmes, D. R.; Bunn, C. W.; Smith, D. J. The Crystal Structure of Polycapromide: Nylon 6. *J. Polym. Sci.* **1955**, *17*, 159–177.

(66) Arimoto, H.; Ishibashi, M.; Hirai, M.; Chatani, Y. Crystal Structure of the γ -Form of Nylon 6. *J. Polym. Sci., Part A: Gen. Pap.* **1965**, *3*, 317–326.

(67) Ziabicki, A. Über die Mesomorphe β -Form von Polycapronamid und Ihre Umwandlung in die Kristalline Form α . *Colloid Polym. Sci.* **1959**, *167*, 132–141.

(68) Penel-Pierron, L.; Depecker, C.; Séguéla, R.; Lefebvre, J. M. Structural and Mechanical Behavior of Nylon 6 Films Part I. Identification and Stability of the Crystalline Phases. *J. Polym. Sci., Part B: Polym. Phys.* **2001**, *39*, 484–495.

(69) Liu, Y.; Cui, L.; Guan, F.; Gao, Y.; Hedin, N. E.; Zhu, L.; Fong, H. Crystalline Morphology and Polymorphic Phase Transitions in Electrospun Nylon-6 Nanofibers. *Macromolecules* **2007**, *40*, 6283–6290.

(70) Liu, X.; Breen, C. High-Temperature Crystalline Phases in Nylon 6/Clay Nanocomposites. *Macromol. Rapid Commun.* **2005**, *26*, 1081–1086.

(71) Zhang, X.; Fan, X.; Li, H.; Yan, C. Facile Preparation Route for Graphene Oxide Reinforced Polyamide 6 Composites via *In Situ* Anionic Ring-Opening Polymerization. *J. Mater. Chem.* **2012**, *22*, 24081–24091.

(72) Dresselhaus, M. S.; Jorio, A.; Souza Filho, A. G.; Saito, R. Defect Characterization in Graphene and Carbon Nanotubes Using Raman Spectroscopy. *Philos. Trans. R. Soc., A* **2010**, *368*, 5355–5377.

(73) Skrovanek, D. J.; Howe, S. E.; Painter, P. C.; Coleman, M. M. Hydrogen Bonding in Polymers: Infrared Temperature Studies of an Amorphous Polyamide. *Macromolecules* **1985**, *18*, 1676–1683.

(74) Rotter, G.; Ishida, H. FTIR Separation of Nylon-6 Chain Conformations: Clarification of the Mesomorphous and γ -Crystalline Phases. *J. Polym. Sci., Part B: Polym. Phys.* **1992**, *30*, 489–495.

(75) Quarti, C.; Milani, A.; Civalieri, B.; Orlando, R.; Castiglioni, C. *Ab Initio* Calculation of the Crystalline Structure and IR Spectrum of Polymers: Nylon 6 Polymorphs. *J. Phys. Chem. B* **2012**, *116*, 8299–8311.

(76) Liu, X.; Wu, Q.; Berglund, L. A.; Fan, J.; Qi, Z. Polyamide 6-Clay Nanocomposites/Polypropylene-Grafted-Maleic Anhydride Alloys. *Polymer* **2001**, *42*, 8235–8239.

(77) Karsli, N. G.; Aytac, A. Tensile and Thermomechanical Properties of Short Carbon Fiber Reinforced Polyamide 6 Composites. *Composites, Part B* **2013**, *51*, 270–275.

(78) Krevlen, D. W. V. *Properties of Polymers*, 3rd ed.; Elsevier: New York, 1990; p 203.

(79) Xie, P.; Li, Y.; Hou, Q.; Sui, K.; Liu, C.; Fu, X.; Zhang, J.; Murugadoss, V.; Fan, J.; Wang, Y.; Fan, R.; Guo, Z. Tunneling-Induced Negative Permittivity in Ni/MnO Nanocomposites by a Bio-Gel Derived Strategy. *J. Mater. Chem. C* **2020**, *8*, 3029–3039.

(80) Koo, E.; Ju, S.-Y. Role of Residual Polymer on Chemical Vapor Grown Graphene by Raman Spectroscopy. *Carbon* **2015**, *86*, 318–324.

(81) Humphrey, W.; Dalke, A.; Schulten, K. VMD: Visual Molecular Dynamics. *J. Mol. Graphics* **1996**, *14*, 33–38.

Flavin Mononucleotide Mediated Formation of Highly Electrically Conductive Hierarchical Monoclinic Multiwalled Carbon Nanotube-Polyamide 6 Nanocomposites

Minsuk Park,[†] Seulki Yoon,[‡] Junmo Park,[†] No-Hyung Park,^{,§} and Sang-Yong Ju^{*,†}*

[†]Department of Chemistry, Yonsei University, 50 Yonsei-ro, Seodaemun-Gu, Seoul 03722, Republic of Korea, [‡]Human Convergence Technology Group, Korea Institute of Industrial Technology, Ansan-Si, Gyeonggi-Do 15588, Republic of Korea, [§]Department of Textile Convergence of Biotechnology and Nanotechnology, Korea Institute of Industrial Technology, Ansan-Si, Gyeonggi-Do 15588, Republic of Korea

* E-mail: nohyung@kitech.re.kr; syju@yonsei.ac.kr

Table of Contents.....	S1
Fig. S1. AFM height images of dFMN-MWNT.....	S2
Fig. S2. Plots of TGAs and corresponding derivatives of weight	S2
Fig. S3. Surface morphologies of nanocomposites	S3
Fig. S4. OM images of pristine PA and xylene-treated PA.....	S3
Fig. S5. SEM images of as-prepared dFMN-MWNT	S4
Fig. S6. Monoclinic arrangement of MWNT in PA-dFMN-MWNT-10.....	S5
Fig. S7. SEM images of MWNT near micro cracks in PA-dFMN-MWNT-10	S6
Fig. S8. SEM images of PA under similar treatment	S7
Fig. S9. HRTEM images and FT images of various polymorphs of PA.....	S7
Fig. S10. Tensile strengths of PA only and nanocomposites	S8
Table S1. Scattering vector, crystal density, and crystalline fraction from GIXRD data.....	S9
Table S2. Determined lattice parameters with minimum errors.....	S10
Cited reference.....	S11

Figure S1. (A-B) AFM height images of dFMN-MWNT on Si wafer. Helical feature of isoalloxazine moiety was observed repetitively on the MWNT surface, and their height difference was about 1 to 2 nm like our last result, according to the reference.^{S1}

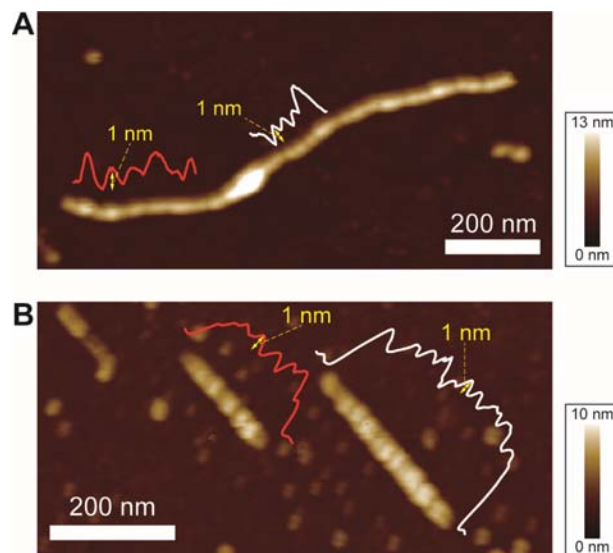


Figure S2. Plots of TGAs (top) and corresponding derivatives of weight (bottom) of (A) FMN (black), dFMN (red), and (B) pre-annealed MWNT (black), and dFMN-MWNT (red). Green arrow and dotted line denote the near middle-point temperature (524 °C) of weight loss by *N*-pentadienyl side chain, and are used to access dFMN content in dFMN-MWNT.

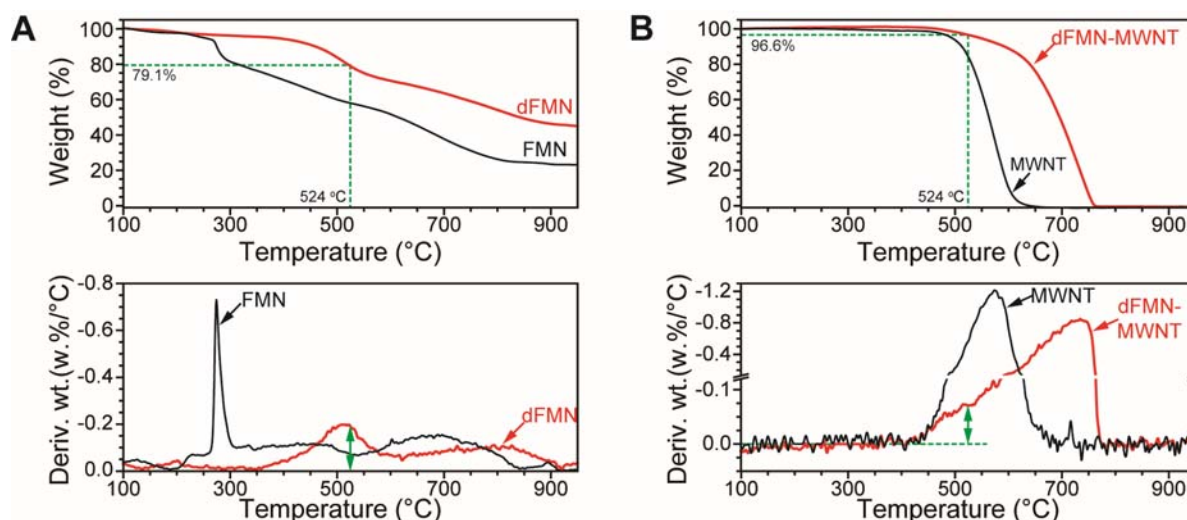


Figure S3. Surface morphologies of nanocomposites. SEM images of (A and B) PA-dFMN-MWNT-1, (C and D) -5, and (E and F) -10 with different magnifications. Yellow dotted area in A indicates a dFMN-MWNT-enriched domain.

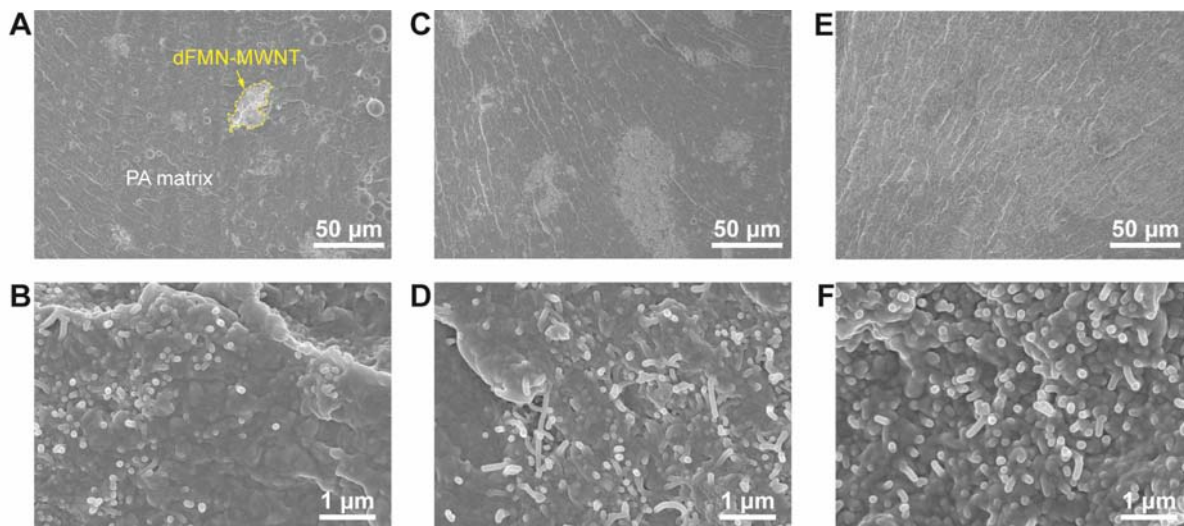


Figure S4. OM images of pristine PA with (A) low and (B) high magnifications, and hot xylene-treated PA (C) low and (D) high magnifications.

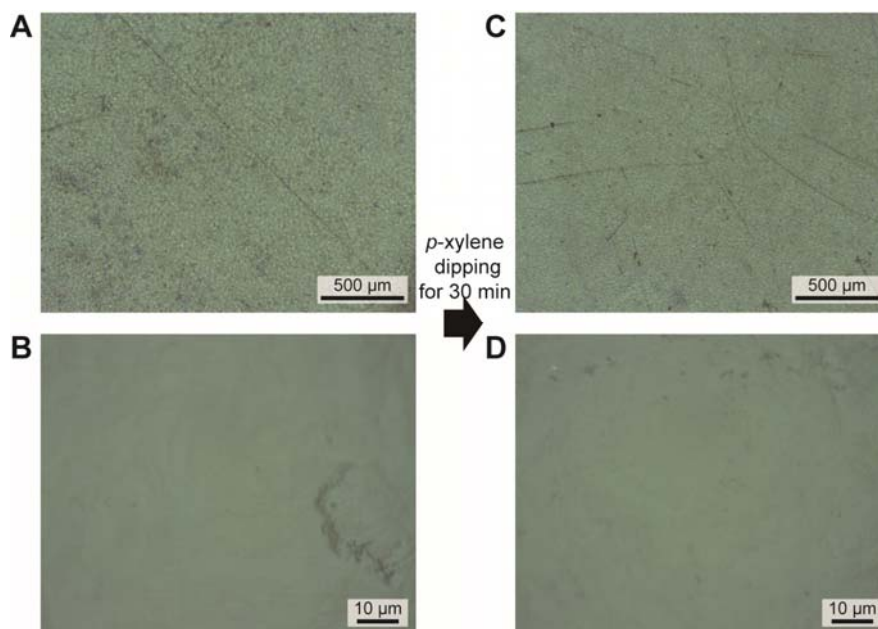


Figure S5. (A-D) SEM images of as-prepared dFMN-MWNT with different magnifications.

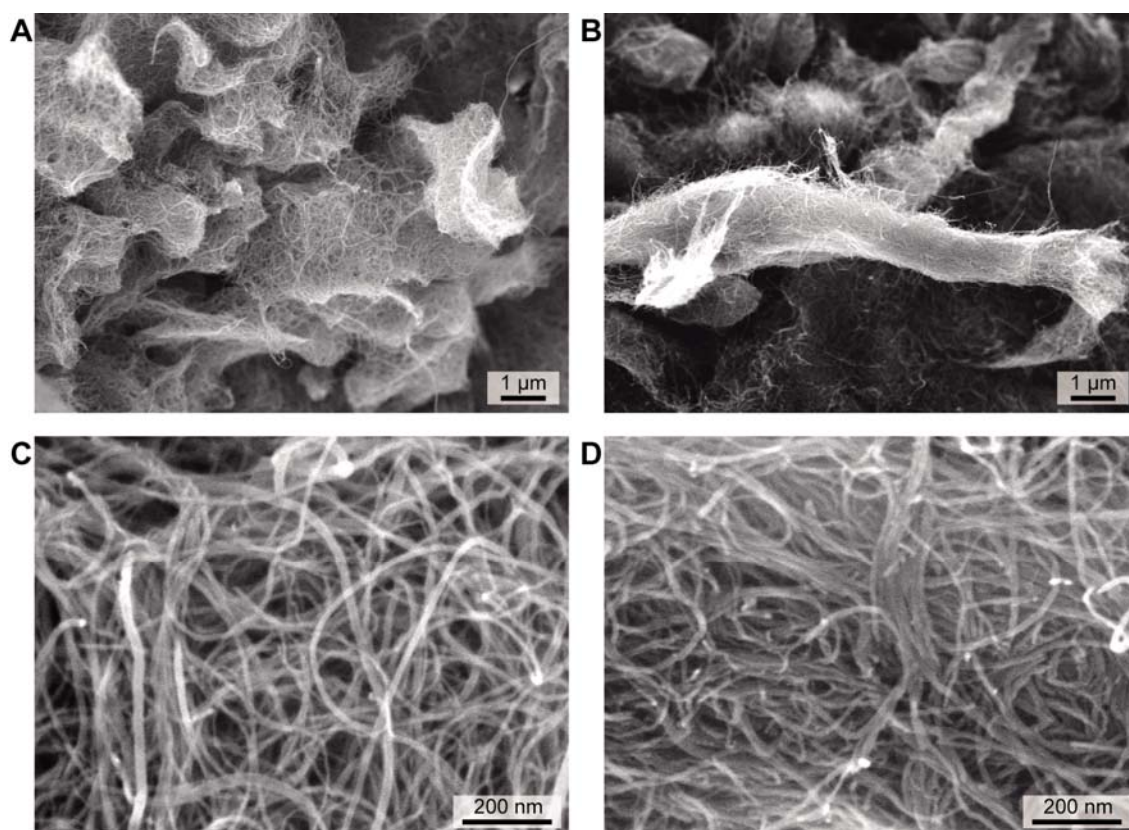


Figure S6. Monoclinic arrangements of MWNT in PA-dFMN-MWNT-10 after hot xylene treatment. (A) SEM images with low magnification and (B-E) corresponding FT images from selected areas marked by dotted boxes in (A). (F) High-magnification SEM image and (G) the corresponding FT image. FT processing from SEM image was conducted with 500×500 nm² region. (A) and (F) are same figures and replicated to show the position-dependent monoclinic shape of MWNT network.

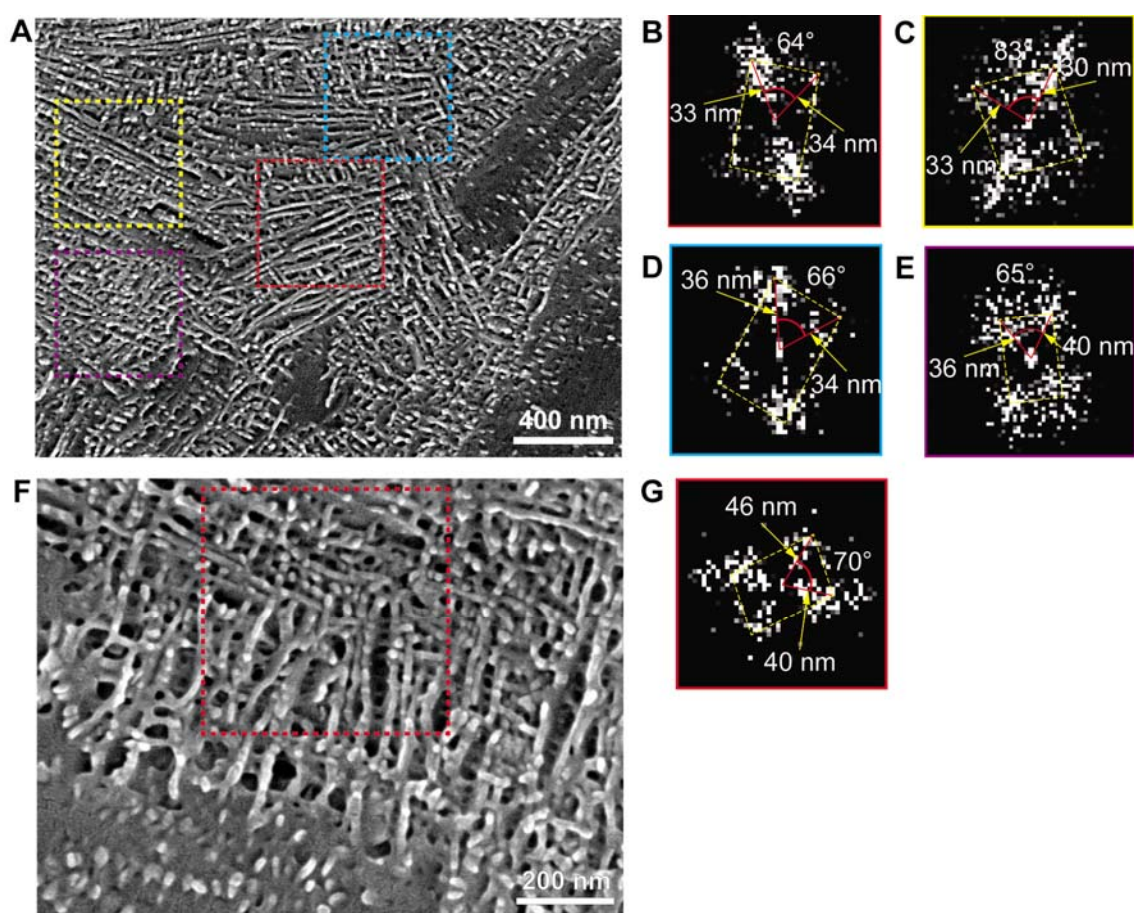


Figure S7. SEM images of MWNT near micro cracks in PA-dFMN-MWNT-10 with (A) low, (B-D) middle, and (E-F) high magnifications.

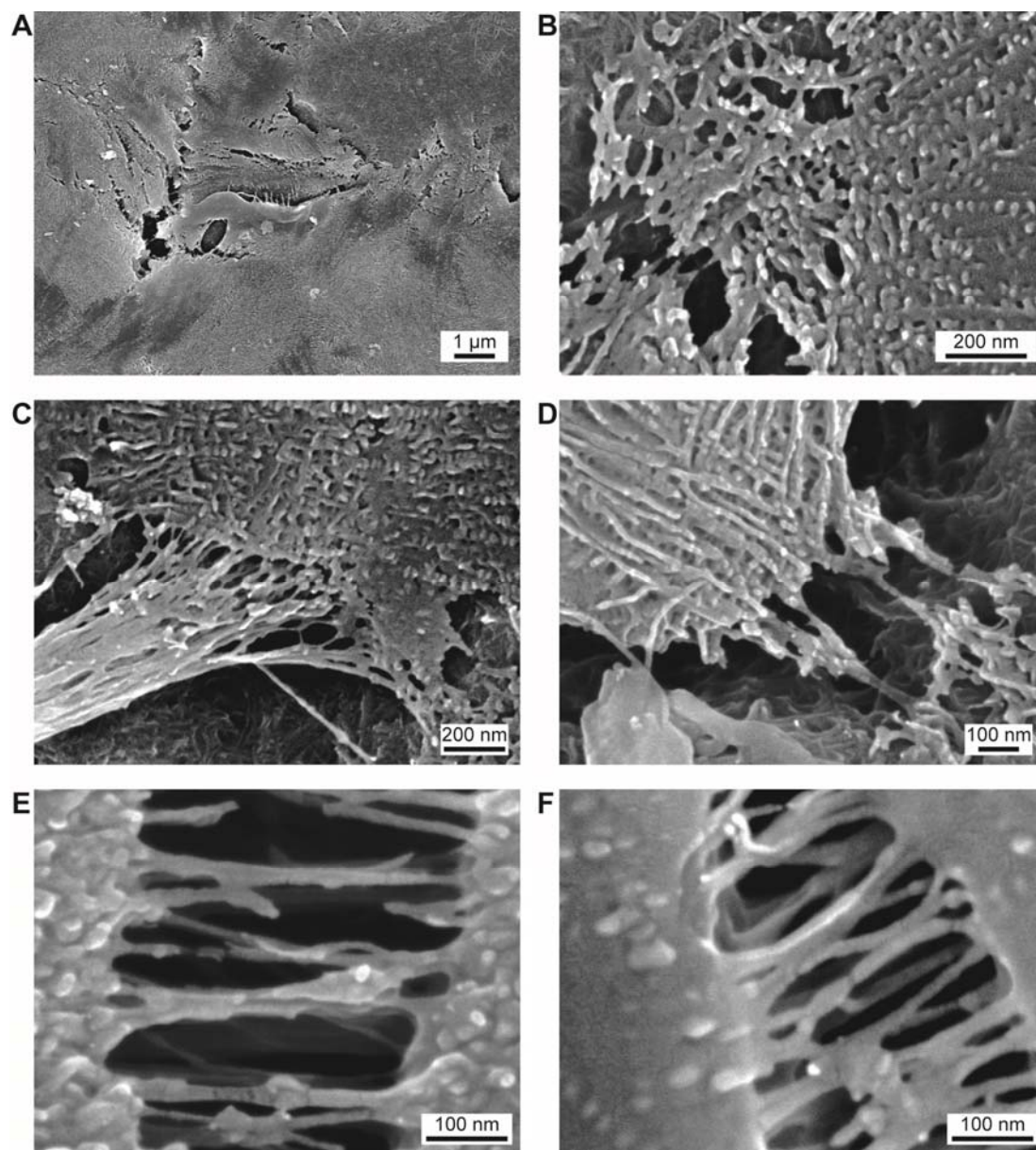


Figure S8. (A-B) SEM images of PA under similar treatment.

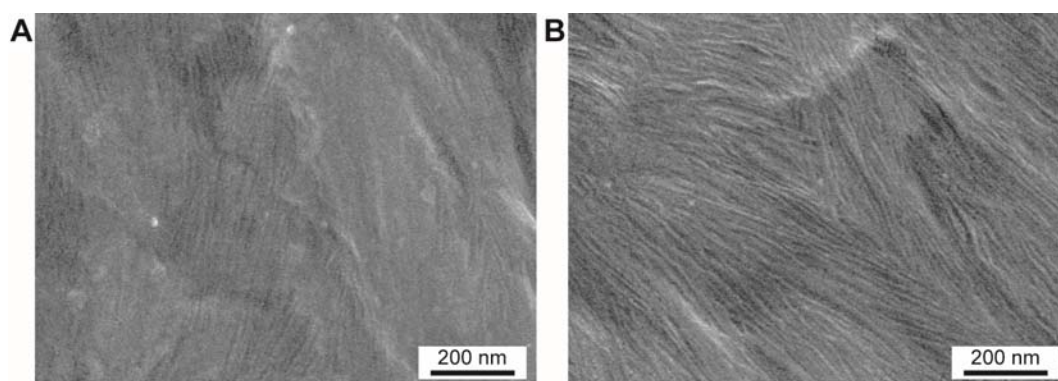


Figure S9. (A-E) HRTEM images and selected-area FT patterns of various polymorphs of PA near MWNT corresponding to yellow, and red regions, respectively.

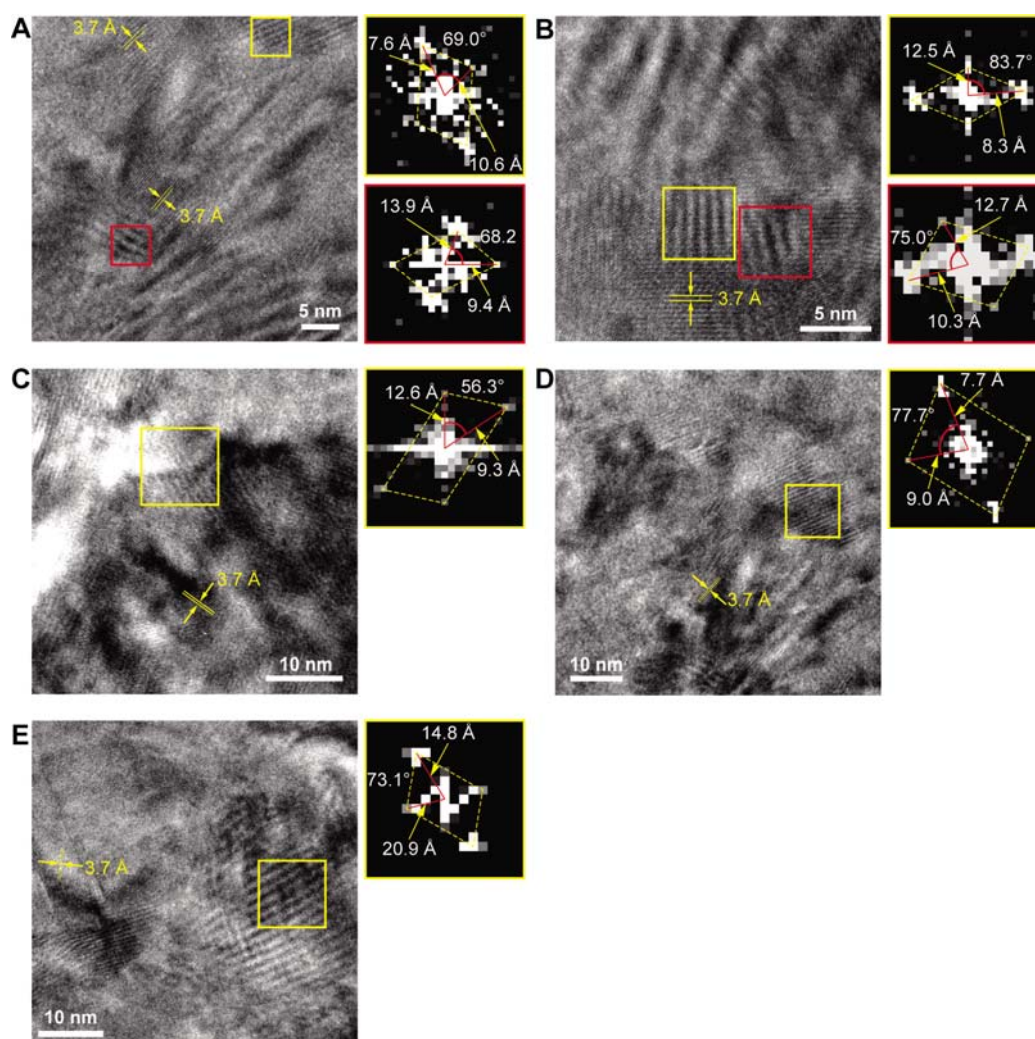


Figure S10. (A) Tensile strengths of PA only and nanocomposites. Error bars were obtained from standard deviation through three separate measurements. (B) Microvoids observed by OM image with transmission mode.

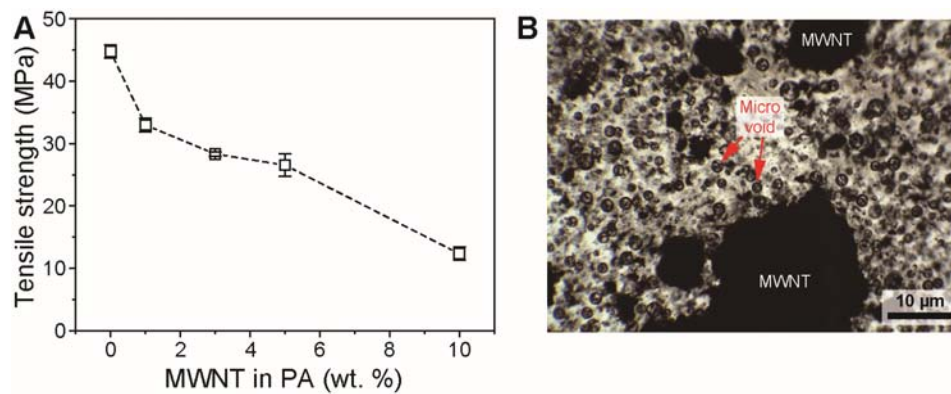
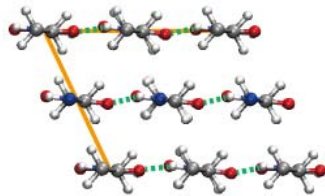
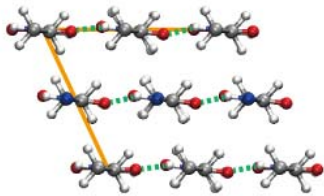
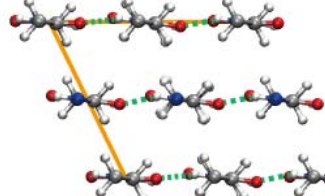
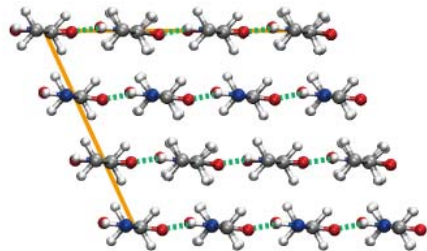


Table S1. Scattering vector q , crystal density ρ , and crystalline fraction from peak GIXRD data deconvoluted by using the Voigt method.

Sample	Polymorphs	PA-based phase				MWNT-induced PA phase			
		α		β	γ	NT- α		NT- α'	
	Reflection (hkl)	(200)	(002)/(202)	-	(020)	(200)	(002)/(202)	(200)	(002)/(202)
PA only	q (nm ⁻¹)	14.30	16.79	15.21	15.48				
	Relative area (a.u.)	115640	95676	54073	21263	-	-	-	-
	Area/unitcell (Å ²)	72.62		-	-	-	-	-	-
	# of repeat unit/unitcell	8		-	-	-	-	-	-
	ρ (g/cm ³)	1.2		-	-	-	-	-	-
	Crystalline fraction (%)	73.7		18.9	7.4				
PA-dFMN-MWNT-10	q (nm ⁻¹)	14.23	16.91	15.98	15.45	13.16	15.00	9.96	11.95
	Relative area (a.u.)	50049	85866	112099	4666	4940	2784	8140	7504
	Area/unitcell (Å ²)	72.36		-	-	88.96		145.89	
	# of repeat unit/unitcell	8		-	-	8		18	
	ρ (g/cm ³)	1.21		-	-	0.98		1.34	
	Crystalline fraction (%)	49.2		40.6	1.7	2.8		5.7	
<i>p</i> -xylene treated PA-dFMN-MWNT-10	q (nm ⁻¹)	14.24	16.91	15.94	15.53	13.16	15.05	9.99	11.96
	Relative area (a.u.)	56707	101013	74418	5467	4104	5101	5466	7477
	Area/unitcell (Å ²)	72.28		-	-	88.67		145.31	
	# of repeat unit/unitcell	8		-	-	8		18	
	ρ (g/cm ³)	1.21		-	-	0.98		1.35	
	Crystalline fraction (%)	60.7		28.7	2.1	3.5		5.0	

Table S2. Determined lattice parameters with minimum errors compared by measured and calculated d spacings.

PA only					PA-dFMN-MWNT-10														
α phase					α phase					NT- α phase					NT- α' phase				
																			
Lattice parameters (monoclinic)					Lattice parameters (monoclinic)					Lattice parameters (monoclinic)					Lattice parameters (monoclinic)				
Lengths (Å)		Angles (°)			Lengths (Å)		Angles (°)			Lengths (Å)		Angles (°)			Lengths (Å)		Angles (°)		
a	9.71	α	90.0		a	9.74	α	90.0		a	10.62	α	90.0		a	13.88	α	90.0	
b	17.2	β	64.8		b	17.2	β	65.1		b	17.2	β	64.0		b	17.2	β	65.4	
c	8.27	γ	90.0		c	8.19	γ	90.0		c	9.32	γ	90.0		c	11.56	γ	90.0	
Reflection			Measured d spacing (Å)	Calculated d spacing (Å)	Reflection			Measured d spacing (Å)	Calculated d spacing (Å)	Reflection			Measured d spacing (Å)	Calculated d spacing (Å)	Reflection			Measured d spacing (Å)	Calculated d spacing (Å)
h	k	l			h	k	l			h	k	l			h	k	l		
2	0	0	4.393	4.391	2	0	0	4.416	4.417	2	0	0	4.776	4.773	2	0	0	6.307	6.310
0	0	2	3.743	3.741	0	0	2	3.715	3.714	0	0	2	4.189	4.188	0	0	2	5.256	5.255
2	0	2	3.743	3.741	2	0	2	3.715	3.716	2	0	2	4.189	4.187	2	0	2	5.256	5.255
Error		0.0015%			Error		0.0005%			Error		0.0016%			Error		0.0015%		

Cited reference

S1. Kim, S.; Jang, M.; Park, M.; Park, N.-H.; Ju, S.-Y., A Self-Assembled Flavin Protective Coating Enhances the Oxidative Thermal Stability of Multi-Walled Carbon Nanotubes. *Carbon* **2017**, *117*, 220-227.